Nanoscale

PAPER

View Article Online
View Journal | View Issue

Cite this: *Nanoscale*, 2025, **17**, 28033

A rapid route to perovskites: barium titanate nanoparticles *via* microwave-assisted solvothermal synthesis

Vinith Johnson, Sunil Vasu and Uday Kumar S *

Barium titanate ($BaTiO_3$) is a perovskite material with remarkable dielectric, ferroelectric, and piezoelectric properties, making it valuable in biomedical and functional devices. Its performance depends on the crystal structure, phase purity, and particle size. Conventional synthesis methods are energy-intensive and less scalable. Microwave-assisted solvothermal synthesis provides a more efficient and scalable alternative, enabling better control over particle characteristics. In this work, $BaTiO_3$ nanoparticles (BTNPs) were prepared using the microwave-assisted solvothermal approach to examine how the reaction time affects their structural and functional behaviour. Detailed characterization revealed that the sample synthesized within 30 minutes achieved the highest crystallinity and the lowest defect density. This sample also exhibited fewer surface-bound organic residues, mainly oxygen-bound metal precursors, compared to other samples. Morphological analysis revealed that the 30 minute synthesis yielded smaller, well-crystallized particles, whereas extending the reaction time led to agglomeration. These observations were further supported by surface potential measurements, which indicated improved colloidal stability. Overall, 30 minutes was identified as the optimal synthesis time, producing BTNPs with superior crystallinity, phase purity, and functional properties. This study underscores the microwave-assisted solvothermal approach as a rapid, energy-efficient, and scalable method to produce high-quality BTNPs for applications in the dielectric, optoelectronic, and biomedical fields.

Received 31st July 2025,
Accepted 5th November 2025

DOI: 10.1039/d5nr03238e

rsc.li/nanoscale

Introduction

$BaTiO_3$, a perovskite material, has emerged as an important material in multilayer ceramic capacitors due to its dielectric properties.[1,2] The increasing demand for miniaturized electronic devices with improved performance has paved the way for the utilization of BTNPs. The variation in the crystal structure leads to diverse properties such as ferromagnetic, piezoelectric, pyroelectric and paramagnetic behaviour. $BaTiO_3$ is well known for its temperature-dependent phase transitions, which significantly influence its crystal structure. Additionally, it is well established that the physical properties such as electrical, mechanical, and dielectric characteristics of polycrystalline materials are intrinsically linked to their grain size. Grain size-dependent phase transitions introduce intriguing material properties, making $BaTiO_3$ one of the most extensively studied and utilized ferroelectric materials.[3,4] Notably, it has been observed that reducing the grain size of polycrystalline $BaTiO_3$ to the micron scale results in a substantial increase in its dielectric constant at room temperature. The dielectric properties of $BaTiO_3$ enable it to serve as an efficient electrical insulator, minimizing charge leakage and preventing dielectric breakdown. This characteristic is crucial for power transmission systems, high-voltage insulation, and the protection of electronic circuits. $BaTiO_3$ further significantly improves the dielectric properties of electronic devices *via* various nanostructured forms of $BaTiO_3$, including nanoparticles, nanowires, and hollow nanostructures. Additionally, the nanoscale dimensions enable better control over the material's phase transitions and polarization behavior, further enhancing its dielectric performance in advanced electronic and optoelectronic devices.[5]

$BaTiO_3$ belongs to the perovskite family, exhibiting a perovskite crystal structure at temperatures below 1460 °C and transitioning to a non-perovskite hexagonal polymorph at higher temperatures. The crystal structure of $BaTiO_3$ is characterized by a primitive cubic unit cell, where the larger A-site cation (typically a monovalent, divalent (Ba^{2+}), or trivalent metal) occupies the corners of the cube, while the smaller B-site cation (such as a pentavalent, tetravalent (Ti^{4+}), or trivalent element) resides at the center of the cube. The oxygen anion typically occupies the center of each face. The perovskite structure can be conceptualized as a three-dimensional framework of TiO_6 octahedra, with Ba^{2+} having a coordination number of 12.[6] The perovskite structure of BTNPs enables it to generate charges when subjected to

Department of Chemical Engineering, Indian Institute of Technology Tirupati, Andhra Pradesh, India. E-mail: udaykumar@iittp.ac.in

mechanical deformation, a phenomenon that arises due to the asymmetric displacement of dipoles within its crystal lattice. This deformation-induced shift in dipoles generates piezoelectricity,[7] making $BaTiO_3$ an appealing material in science and engineering applications. Recent research has increasingly explored the potential of $BaTiO_3$ for applications in the biological and medical fields. Studies have demonstrated its suitability for various biomedical applications, including *in vitro* imaging,[8,9] cell targeting,[10] drug delivery,[11] and its use as a nanotransducer within biological systems.[12,13] Furthermore, its inherent piezoelectric properties enable the generation of electromechanical stimulation, which plays a crucial role in modulating cellular behavior under pathological conditions. This unique characteristic has been extensively leveraged in tissue engineering and regenerative medicine, where $BaTiO_3$-based materials are employed at a significant scale to enhance cellular responses and promote tissue regeneration,[14] and promote osteogenesis and accelerate bone tissue repair in response to mechanical stimuli.[15]

Beyond their well-established dielectric and ferroelectric properties, BTNPs have also exhibited promising electrocatalytic properties, making them potential candidates for electroanalytical applications. For instance, Balamurugan Arumugam *et al.* employed $BaTiO_3$ for electrochemical quantification of quinol, an oncogenic pollutant. The fabricated sensor exhibited a lower limit of detection (LOD) of 0.009 μM due to superior electrical conductivity of $BaTiO_3$.[16] In another study, $BaTiO_3$ nanocubes were employed as an electroactive interface for the detection of acetaminophen and dopamine. The $BaTiO_3$ modified graphitic carbon electrode (GCE) demonstrated a broad linear range of 10–100 μM with a LOD of 0.35 μM for dopamine and 0.23 μM for acetaminophen.[17] It is imperative to note that the enhanced electrochemical properties of BTNP-based sensors are primarily attributed to the physio-chemical properties of BTNPs that include a high surface area to volume ratio, low aggregation, high catalytical activity and ferroelectricity. Notably, all these properties heavily rely on the structure and morphology of BTNPs which indeed are influenced by the synthesis route. Hence, choosing an optimal synthesis route is crucial for enabling optoelectronic and electroanalytical applications of BTNPs.

The conventional methods for synthesizing $BaTiO_3$ typically involve solid-state reactions at high temperature annealing to attain specific phase formation and crystallization. For instance, $BaTiO_3$ powders can be produced through a high-energy ball milling process, where mixtures of $BaCO_3$ and TiO_2 powders are mechanically ground to reduce the particle size and enhance homogeneity before undergoing high-temperature annealing to induce the formation of the desired perovskite phase.[18] Alternatively, when BaO and TiO_2 are used as starting materials, a mechanochemical reaction initiated by the intense energy input during ball milling can directly yield $BaTiO_3$.[19] However, these solid-state methods are often limited by drawbacks such as contamination from milling media and inhomogeneous particle size distribution, which directly impact the functional properties of the resulting BTNPs.

To address these limitations, several chemical synthesis methods have been developed, including solvothermal,[20] hydrothermal[21–25] and sol–gel techniques,[26,27] and co-precipitation methods with oxalates[28–30] and catecholates,[31] which have been employed to prepare $BaTiO_3$ powders from various barium and titanium cation precursor solutions. These methods enhance control over critical parameters such as particle size, morphology, and chemical homogeneity – factors that are essential for tuning the crystal structure, phase purity, and dielectric properties of BTNPs.[32] Among these, the microwave-assisted solvothermal method stands out due to its ability to rapidly induce nucleation and crystallization, offering finer control over nanoparticle growth kinetics. Moreover, the method improves the stability of nanoparticle synthesis, shortens processing times, and reduces energy consumption, owing to the efficient dielectric heating mechanism of microwaves that accelerates reaction rates and enhances thermal uniformity.[5,33]

In this study, we assessed the structural and morphological characteristics of BTNPs synthesized *via* microwave-assisted solvothermal methods at different time intervals—10, 20, 30, and 40 minutes—under constant temperature conditions. The resulting BTNPs were analysed for their size distribution, crystallinity, and phase purity, all of which are critical for optimizing their dielectric performance. This rapid and energy-efficient synthesis method offers a promising approach for producing high-quality BTNPs with enhanced uniformity and functional properties, making them suitable for use in advanced electronic devices and energy storage applications.

Materials and methods

Materials

Titanium butoxide ($Ti(C_4H_9O)_4$, 99% purity) and poly(vinylidene fluoride) (PVDF, average $M_w \sim 534\,000$ daltons by GPC) were purchased from Sigma-Aldrich. Analytical grade barium hydroxide octahydrate ($Ba(OH)_2{\cdot}8H_2O$) and potassium hydroxide (KOH) were purchased from SRL. Anhydrous ethanol (CH_3CH_2OH, 99.9% purity, Merck), deionized water (dH_2O), and nitric acid (HNO_3, 65%, Merck) were used for the synthesis. The indium tin oxide coated glass substrate (ITO) was purchased from Shilpent Enterprises, India. Sodium chloride (NaCl), potassium chloride (KCl), potassium ferricyanide ($K_3[Fe(CN)_6]$), sodium diphosphate anhydrous [Na_2HPO_4], potassium phosphate monobasic [NaH_2PO_4], and *N*-methyl-2-pyrrolidone (NMP) were sourced from SRL, India.

Synthesis of titanium dioxide sol

Titanium dioxide (TiO_2) sol was prepared through the hydrolysis method. The sol preparation was carried out at a molar ratio of 1 : 15 : 0.3 : 4 of $Ti(C_4H_9O)_4$, CH_3CH_2OH, HNO_3, and dH_2O, respectively. Briefly, 2.62 mL of $Ti(C_4H_9O)_4$ was mixed with 6.73 mL of CH_3CH_2OH under continuous stirring at 0 °C using an ice bath to form solution A. Solution B was prepared by mixing 1 mL of ethanol with 0.56 ml of dH_2O, along with 0.146 mL of HNO_3.

Subsequently, solution B was added dropwise to solution A while maintaining the reaction mixture at 0 °C to control the reaction rate and prevent hydrolysis exothermicity for a duration of 5 minutes. The formation of an opaque sol indicated the successful hydrolysis and formation of TiO_2 sol. The experiments were repeated in triplicate to ensure the reproducibility of the TiO_2 sol.

Earlier reports indicate that the impact of precursor concentration on the rate of hydrolysis and condensation reaction is amplified with an increase in mass fraction of $Ti(C_4H_9O)_4$, resulting in a shorter time to generate TiO_2, and decreases the precursor utilization efficiency. Also, a higher mass fraction of the precursor is more sensitive to water, leading to a more violent reaction that can make the reaction less complete.[34,35]

Synthesis of BTNPs

To synthesize BTNPs, 5 ml of the prepared TiO_2 sol was mixed with 0.152 M of $Ba(OH)_2{\cdot}8H_2O$ (*i.e.*, 1.104 g of $Ba(OH)_2{\cdot}8H_2O$, dissolved in 23 ml of dH_2O). This mixture resulted in the formation of a white precipitate, which was stirred until a homogeneous suspension was achieved. The pH of the solution was then adjusted to 13 using a 5 M KOH solution. The resulting solution was then transferred to a silicon carbide reaction tube and subjected to microwave synthesis at 180 °C for 30 minutes using a microwave reactor (Monowave 450 from Anton Paar). The overall synthesis procedure is shown in Fig. 1. After synthesis, the suspension was centrifuged at 6000 RPM for 20 minutes to separate nanoparticles from the liquid. The supernatant was discarded, and the pellet was washed 2–3 times with deionized water and ethanol to remove any residual salts and unreacted chemicals. The final product was then dried in a hot air oven at 50 °C for 24 hours to obtain BTNPs.

Characterization of $BaTiO_3$

The formation of BTNPs was confirmed with the help of multiple characterization techniques. The crystal structure of BTNPs was analysed using a Malvern Panalytical X-ray diffractometer (XRD) (Aeris, UK), with 2θ measurements taken between 10° and 90° with a step size of 0.01087 and at a speed of 29.07 times per step using the Cu Kα radiation source. The baseline correction and peaks were identified using X'Pert HighScore Plus. Attenuated Total Reflectance–Fourier Transform Infrared Spectroscopy (ATR-FTIR) was performed with a Spectrum II spectrometer (PerkinElmer, USA) with the spectra recorded over the wavenumber range of 400 to 2000 cm^{-1}. Thermal stability of the BTNPs was assessed *via* thermogravimetric analysis (TGA) using a Hitachi STA200 Japan thermal analysis system, with measurements conducted from 30 °C to 900 °C at a heating rate of 10 °C min^{-1}. The analysis was performed with nitrogen as the protective gas to avoid oxidation with a flow rate of 100 ml min^{-1}. A Scanning Electron Microscope (SEM) (Zeiss, Germany) equipped with an Energy Dispersive X-ray (EDX) detector was employed to analyse the particle morphology and structural uniformity of BTNPs along with elemental composition with an accelerating voltage of 15.00 kV. All samples were coated with a thin layer of gold by sputtering for 60 seconds at a rate of 30 mA before performing the imaging. The hydrodynamic

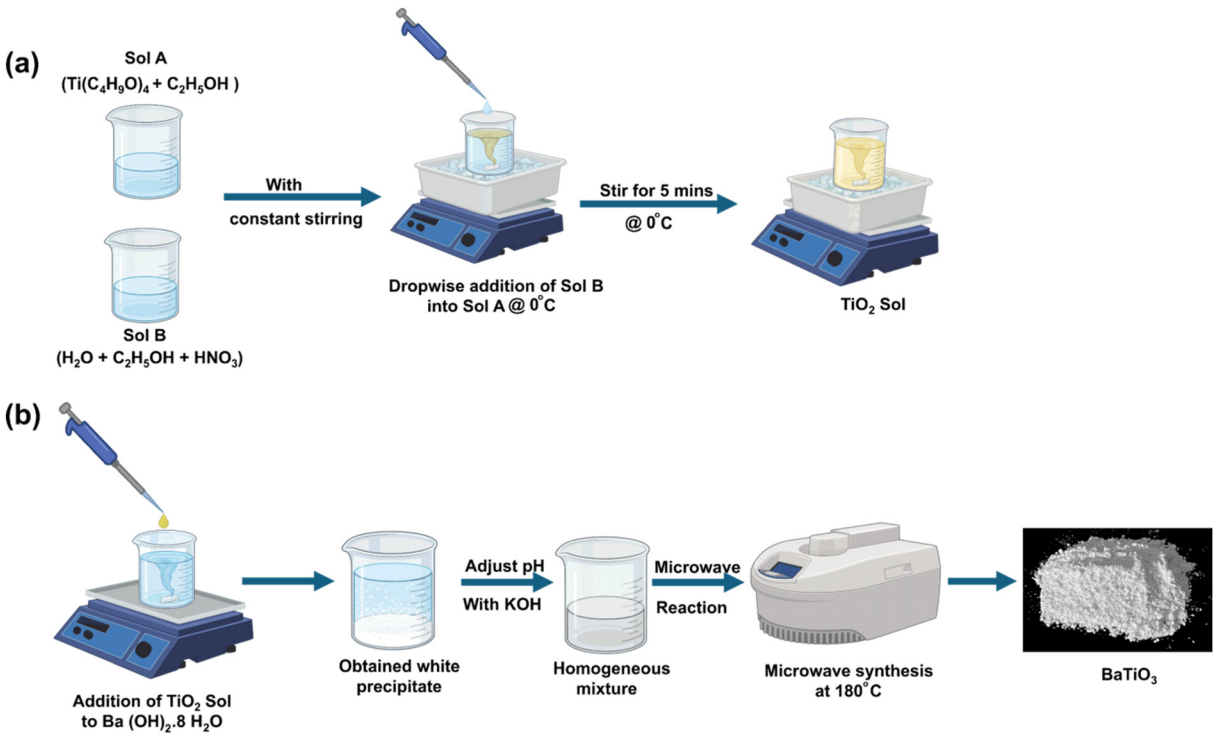

Fig. 1 Schematic representation of $BaTiO_3$ synthesis. (a) TiO_2 sol formation. (b) $BaTiO_3$ synthesis.

particle size and surface potential were measured using Dynamic Light Scattering (DLS) at 25 °C with a Litesizer 500 (Anton Paar, Austria). For the particle size analysis, the samples were dispersed in ethanol. The bandgap of the nanoparticles was determined from UV/Visible-Near Infrared (UV-NIR) absorbance spectra using a Shimadzu instrument. Raman spectroscopy was utilized to analyze the vibrational modes and structural properties of the synthesized BTNPs. Spectra were recorded over a range of 50 cm^{-1} to 1000 cm^{-1} using a LabRAM HR Evolution Raman spectrometer. High-Resolution Transmission Electron Microscopy (HR-TEM) analysis was performed using a JEM-2100Plus instrument (JEOL, Japan) with an accelerating voltage of 200 kV. X-ray photoelectron spectroscopy (XPS), also referred to as electron spectroscopy for chemical analysis (ESCA), was performed using a PHI 5000 VersaProbe III system (Physical Electronics, Japan) to investigate the elemental composition and oxidation states of the material. The spectra were recorded with Al Kα radiation (1486.6 eV, 24.92 W) as the excitation source at a 45° incident angle. Data processing, including background subtraction and peak deconvolution, was carried out using OriginPro software. The electrochemical measurements were conducted using a CHI-760E electrochemical workstation (CH Instruments, USA). Cyclic voltammetry (CV) was employed to assess the electrochemical properties of BTNPs. BTNPs were deposited onto ITO through drop casting, as reported elsewhere.[36] Briefly, 50 mg of BTNPs was dispersed in 200 μL of NMP followed by addition of the PVDF binder (5 mg). The mixture was subjected to bath sonication for 30 minutes to obtain uniform dispersion. Subsequently 50 μL of the resulting mixture was drop casted onto the ITO electrode and air dried at 80 °C for 12 hours. CV experiments were carried out by ramping/sweeping the potential from −0.8 to +0.8 V at a scan rate of 0.05 V s^{-1}. All measurements were carried out in a conventional three-electrode electrochemical cell with indium tin oxide (ITO) as the working electrode, Ag/AgCl (3 M KCl) as the reference electrode and a platinum wire as the counter electrode. Potassium ferricyanide ($K_3[Fe(CN)_6]$) prepared in PBS (1×, pH 7) was used as the redox probe and supporting electrolyte for CV studies.

Results

Crystal structure elucidation through XRD

Fig. 2 presents the XRD patterns of BTNPs synthesized *via* the microwave solvothermal method at 180 °C for different reaction times.

The characteristic diffraction peaks corresponding to the cubic and tetragonal phases of $BaTiO_3$ are typically distinguishable by peak splitting at $2\theta = 45°$, where the tetragonal phase exhibits a split in the (200) reflection, serving as a key marker of the phase transition.[37–39]

In this study, no such peak splitting was observed at $2\theta = 45°$, indicating the absence of the tetragonal phase. Instead, a single sharp reflection corresponding to the (200) plane suggests that the synthesised BTNPs predominantly crystallize

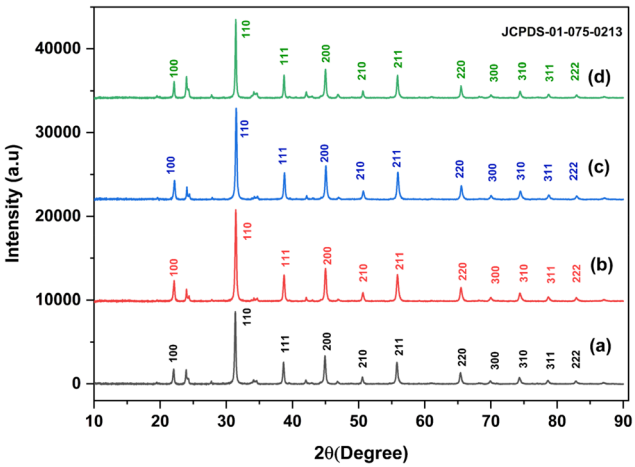

Fig. 2 XRD patterns of the $BaTiO_3$ samples synthesized using the microwave solvothermal method at 180 °C for (a) 10 minutes, (b) 20 minutes, (c) 30 minutes, and (d) 40 minutes.

in the cubic phase. Notably, the diffraction pattern of the sample synthesized for 30 minutes shows increased peak intensity, indicative of enhanced crystallinity, likely due to improved atomic ordering and reduced defect density because of the prolonged synthesis time. Furthermore, the increased intensity could also indicate a reduction in secondary phases or impurities, which might have been present in samples with shorter reaction times. Longer reaction times may allow for stress relaxation within the crystal lattice, leading to sharper peaks and improved crystallinity.

The XRD pattern of the synthesized BTNPs exhibits characteristic peaks at 2θ values of 22.1°, 31.4°, 38.7°, 45.1°, 50.7°, 55.9°, and 65.5°, corresponding to the (100), (110), (111), (200), (210), (211), and (220) crystallographic planes, which are, respectively, in accordance with the standard diffraction pattern of cubic $BaTiO_3$. Additional diffraction peaks observed in the BTNPs at 24°, 34°, and 42° could be indexed to barium carbonate ($BaCO_3$), a commonly reported impurity in the hydrothermal synthesis of $BaTiO_3$.[40–44] The emergence of $BaCO_3$ is from the remarkable surface reactivity of BTNPs with atmospheric CO_2 on BaO-terminated surfaces.[45] In addition, the peak at 47° may arise from secondary TiO_2 phases, which are predominantly associated with the anatase phase.[46,47]

The crystallite size (D) of BTNPs synthesized at various reaction times was estimated using Scherrer's equation.[48,49]

$$D = \frac{k \cdot \lambda}{\beta \cos\theta}$$

where D is the crystallite size, λ is the X-ray wavelength, β is the full width at half maximum (FWHM) of the diffraction peak, θ is the Bragg angle, and k is the shape factor, taken as approximately 0.91. The crystallite sizes calculated from individual diffraction peaks were averaged for each sample. The mean crystallite sizes for BTNPs synthesized at 10, 20, 30, and

40 minutes were approximately 22 nm, 21 nm, 20 nm, and 23 nm, respectively. Among these, the sample synthesized at 30 minutes exhibited the highest degree of crystallinity, suggesting that this condition favoured improved crystal formation.

Analysis of chemical bond vibrations and composition

The ATR-FTIR spectrum of BTNPs is presented in Fig. 3. Infrared spectra were recorded for all samples synthesized at different time intervals, with prominent peaks observed across all four samples.

The characteristic peaks observed between 510–550 cm^{-1} and 415–440 cm^{-1} correspond to the stretching and bending of Ti–O bonds.[50,51] The precise position of Ti–O vibrational modes is known to be sensitive to the crystallographic phase of $BaTiO_3$, exhibiting characteristic shifts depending on whether the material adopts a cubic or tetragonal structure. In the present study, all synthesized BTNPs exhibited features consistent with the cubic phase, as evidenced by the absence of phase-splitting and the symmetry of the peaks in the XRD patterns. These peaks are consistent with the vibrational modes of titanium–oxygen octahedra within the $BaTiO_3$ crystal lattice. A broad absorption band observed in the range of 1620–1650 cm^{-1} is assigned to O–H bending vibrations H–O–H, typically associated with adsorbed water molecules. This feature likely arises from the interaction of metal oxides with atmospheric moisture. Additionally, the presence of this band may be attributed to the formation of water of crystallization in the BTNPs, potentially resulting from the use of hydrates during synthesis.[52]

Additional peaks in the range of 1055–1065 cm^{-1} are indicative of Ti–O linkages or C–O stretching vibrations, possibly resulting from residual TiO_2.[53] In the sample synthesized for 10 minutes, additional peaks were observed: the peak at 1115 cm^{-1} suggests the C–O groups attached to Ti particles,[54] while the peak at 1180 cm^{-1} is attributed to C–O stretching vibrations, possibly from alcohols.

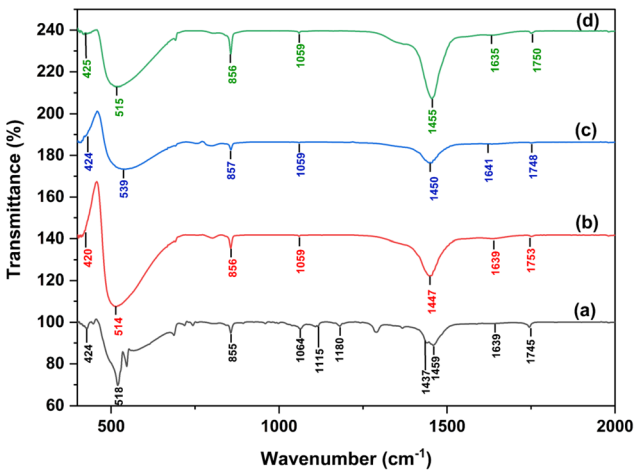

Fig. 3 FTIR spectra of $BaTiO_3$ synthesized at (a) 10 minutes, (b) 20 minutes, (c) 30 minutes, and (d) 40 minutes.

Determination of the optical band gap and absorption characteristics

The UV-NIR absorbance spectra of BTNPs synthesized at varying time intervals are shown in Fig. 4. All samples showed maximum absorbance within the range of 200–400 nm.

The absorbance data were used to determine the optical bandgap energy (E_g) using the Tauc relation:

$$(\alpha h\nu)^{1/n} = A(h\nu - E_g)$$

where α is the absorption coefficient, A is a proportionality constant, ν is the transition frequency, E_g is the bandgap energy, and n in the exponent indicates the nature of the electronic transition and takes values of 1/2 and 2 for direct and indirect bandgaps. As shown in Fig. 4, we observed the best fit for n = 1/2, implying direct electron transitions in the synthesized BTNPs. The optical bandgap of $BaTiO_3$ was calculated by extrapolating the plot of [energy (eV) *vs.* $(\alpha h\nu)^2$] to intercept the energy axis,[41] as shown in Fig. 3. The bandgap of BTNPs synthesized at 10 minutes was found to be 3.209 eV which decreased to 3.126 eV and 3.127 eV at the synthesis time 20 and 30 minutes followed by an increase to 3.145 eV at 40 minutes. The results indicate that the bandgap energy of the nanoparticles decreased with increasing synthesis time up to 30 minutes. The variation in the band gap is due to the crystallinity and defect density in nanomaterials. The prolonged synthesis time enhances crystallinity and structural ordering, which contributes to a slight reduction in band gap energy.[55,56] Conversely, shorter synthesis durations may introduce a higher density of structural defects or amorphous phases, thereby widening the band gap. With continued synthesis, the progressive reduction in defect density results in a further narrowing of the band gap.[55,57] However, after 30 minutes of synthesis, the bandgap started to increase again, likely due to agglomeration or growth of larger particles.

The observed reduction in E_g can be explained by considering oxygen and barium vacancies, which lead to the formation of midgap defect states and consequently result in a reduction of the band gap.[58] The further increase of E_g, 3.145 eV in BTNPs synthesized at 40 minutes, can be attributed to the absence of barium vacancies. However, it still remains lower than that of BTNPs at 10 minutes, likely due to more oxygen vacancies present at 40 minutes.[59] The findings align well with the XPS findings, indicating a significant effect of oxygen and barium vacancies on the optical properties of $BaTiO_3$.

Additionally, the presence of such vacancies results in an absorption tail just below the band gap edge, which is called the Urbach tail. The energy associated with the Urbach tail is termed the Urbach energy, which represents the structural disorder in any crystal lattice. It can be quantified by using the following equation:

$$\alpha = \alpha_0 \exp(h\nu/E_u)$$

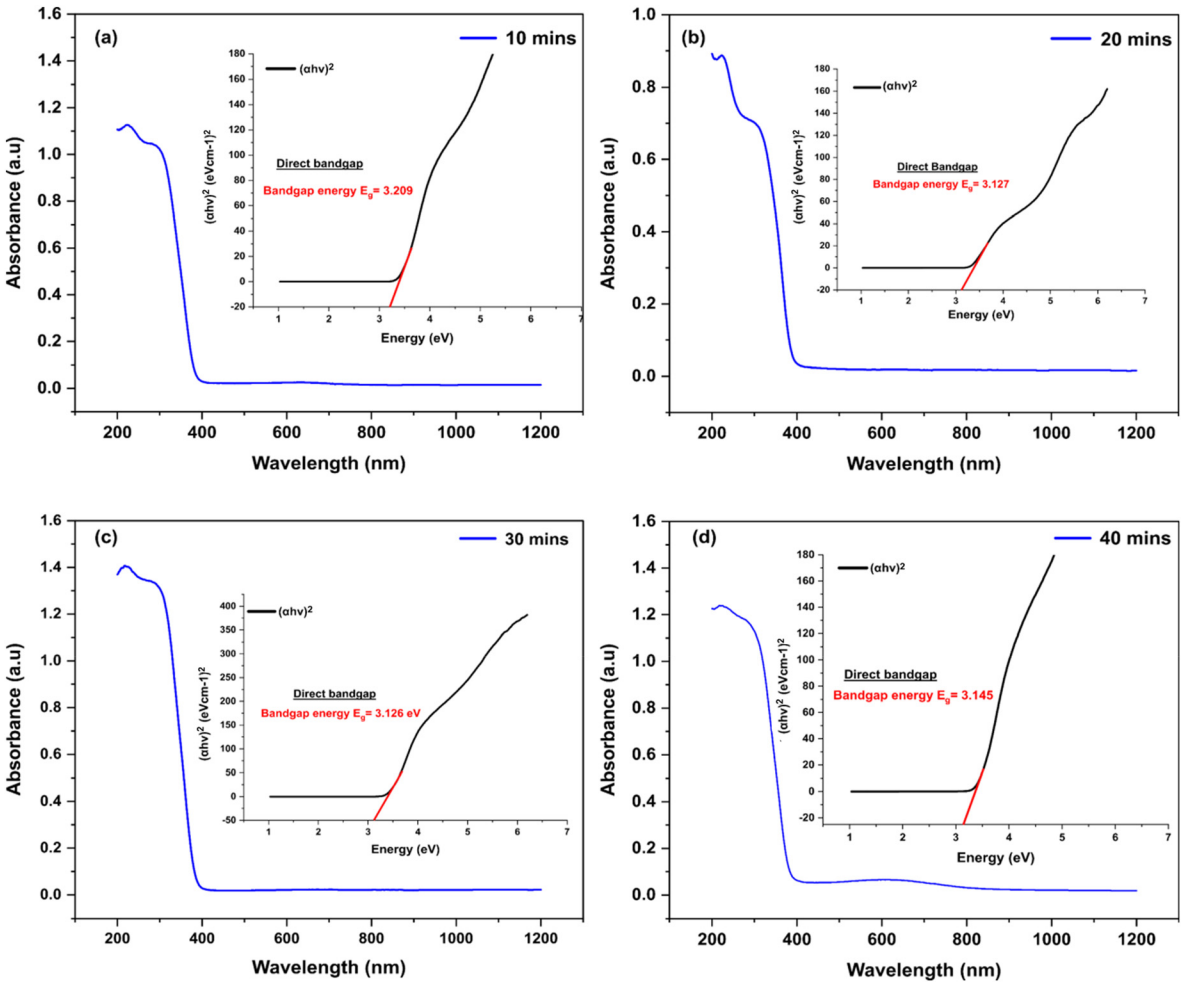

Fig. 4 UV-NIR absorbance spectra of BTNPs synthesized at (a) 10 minutes, (b) 20 minutes, (c) 30 minutes, and (d) 40 minutes.

where α_0 is a constant of proportionality and E_u is the Urbach energy. The Urbach energy can be determined by finding the inverse of the slope of the linear regression in the plot of ln (α) against photon energy, which determines the Urbach plot. The Urbach plot for all the BTNPs is shown in Fig. S1. The E_u for BTNPs synthesized at 10 minutes was determined to be 109 meV which increased to 117 meV at 20 minutes, most likely due to point defects induced by barium and oxygen vacancies.[58,60] The E_u decreased to 100 meV for the BTNPs at 30 minutes as both the barium and oxygen vacancies decreased, enhancing the structural order. The further increase to 163 meV at 40 minutes can be attributed to reintroduction of oxygen vacancies that causes broadening of the Urbach tail.[60] The Urbach analysis corroborates well with the XPS findings. Altogether, varying the microwave processing time influences barium and oxygen vacancies and consequently the optical properties of BTNPs.

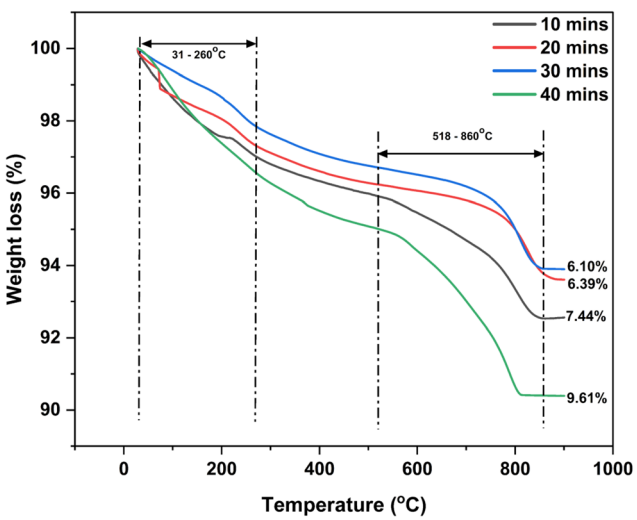

Fig. 5 TGA curves of $BaTiO_3$ at different synthesis times.

Evaluation of thermal stability and decomposition behavior

Fig. 5 presents the TGA curves of the synthesized BTNPs, with thermal stability assessed over the temperature range of 30 °C to 900 °C. The TGA curves for all samples exhibit two distinct stages of weight loss. The first weight loss, occurring between room temperature and 260 °C, is attributed to the release of adsorbed moisture and the breakdown of organic compounds

unstable at elevated temperatures.[61] This implies that the surface of the BTNPs contains a considerable amount of moisture, which aligns with ATR-FTIR and could play a role in influencing the nanoparticle's surface chemistry, especially in applications such as catalysis or dielectric materials where surface properties are critical. The lower weight loss in the 30 minute sample suggests a more complete crystallization process, potentially leading to a reduced number of surface defects or hydroxyl groups.

The second stage of weight loss, observed between 630 °C and 860 °C, is associated with the decomposition of the OH groups chemically linked to Ba–O and Ti–O within the $BaTiO_3$ lattice. Specifically, the dehydroxylation of Ba–O bonds occurs at lower temperatures, while the removal of Ti–O-bound hydroxyl groups requires higher temperatures due to the stronger bond dissociation energies.[62] The removal of oxygen vacancies or other lattice defects could contribute to the observed weight loss in this temperature regime. All samples remained stable above 900 °C, indicating the complete removal of residual organic compounds and precursors. Notably, the sample synthesized for 30 minutes showed the smallest percentage of weight loss, which suggests improved crystallinity and higher phase purity. The reduced weight loss for the sample synthesized for 30 minutes could be an indicator of fewer lattice defects, as the prolonged synthesis time allows for better densification and crystallization of the nanoparticles. This also suggests improved structural ordering, as indicated by the lower dehydroxylation rates. This observation aligns with the XRD results, further supporting the conclusion that this sample has undergone more complete crystallization and densification.

Spectral characterization of phonon and lattice vibrations

Raman spectroscopy was employed to identify phase transitions and quantify impurity phases in the BTNPs. It is well established that $BaTiO_3$ with a tetragonal crystal structure (space group *P4mm*) exhibits characteristic Raman-active vibrational modes, specifically A_1(1TO), A_1(2TO), E(2TO), A_1(3TO), and A_1(3LO)/E(LO).[63] In contrast, the cubic phase (space group $Pm\bar{3}m$) is Raman-inactive due to the isotropic distribution of electrostatic forces, attributed to the high-symmetry octahedral environment (O_h symmetry) surrounding the Ti^{4+} ions within the TiO_6 octahedra.[64,65] However, the presence of oxygen vacancies and other lattice defects disrupts the local cubic symmetry, thereby relaxing selection rules and activating Raman modes even in the cubic phase. Such behaviour is well established in perovskite oxides, including $BaTiO_3$ and related materials.[66,67] In addition, the Raman spectra of these nanoparticles may also indicate the presence of a non-dominant tetragonal phase or pseudo-cubic structure, which has its own Raman-active modes. The presence of these modes provides evidence of the deviation from the pure cubic phase due to the presence of local structural distortions in the crystal structure.[68,69]

The Raman spectra of the $BaTiO_3$ samples were recorded in the range of 50–1000 cm^{-1}, as presented in Fig. 6.

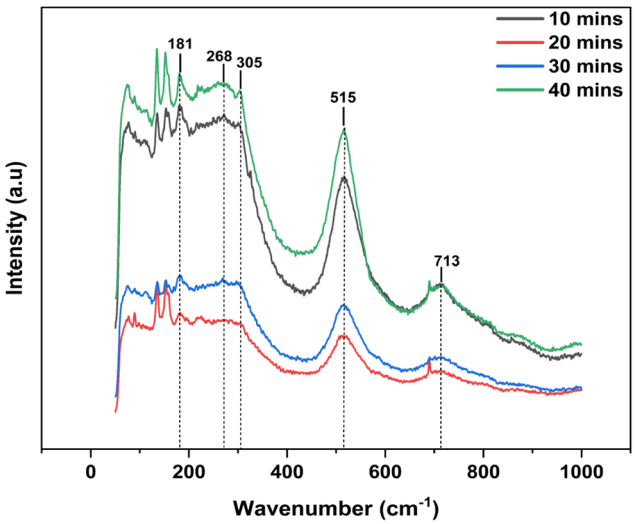

Fig. 6 Raman spectra of $BaTiO_3$ synthesized at different time durations.

Distinct Raman shifts observed at 181, 268, 305, 515, and 713 cm^{-1} correspond to the characteristic vibrational modes of $BaTiO_3$. The broad peaks at 270 and 305 cm^{-1} are attributed to vibrations within the TiO_6 octahedral groups, which are fundamental structural units in $BaTiO_3$.[41] The additional peaks observed in the 120–150 cm^{-1} range of the Raman spectra do not correspond to the standard Raman-active modes of cubic $BaTiO_3$. Such features are commonly attributed to lattice disorder, structural defects, or B-site vacancies in perovskite materials, which induce local symmetry breaking and allow otherwise inactive modes to appear in the Raman spectra.[67]

The Raman peaks observed for BTNPs at 181, 305, 515, and 713 cm^{-1} were attributed to the following vibrational modes: A1(TO) and E(LO) at 181 cm^{-1}; B1 and E(TO + LO) at 305 cm^{-1}; A1(TO) and E(TO) at 515 cm^{-1}; and A1(LO) and E(LO) at 713 cm^{-1}.[70] The peak at 514 cm^{-1} is associated with displacement of oxygen atoms[41] within the Ti–O framework, reflecting the local distortions of the octahedral environment. The absence of a distinct peak at 305 cm^{-1}, which is characteristic of the tetragonal phase, in Fig. 5 indicates that the tetragonal phase is not dominant in the synthesized BTNPs. This suggests that the powders predominantly exhibit a locally symmetric (cubic) environment, with only minor structural distortions.[71]

Measurement of the hydrodynamic diameter and surface potential

Fig. S2 illustrates the hydrodynamic diameter and zeta potential measurement of the synthesized BTNPs. The particle size distribution for all samples shows monodisperse peaks, with a polydispersity index below 0.3, indicating a narrow size distribution and uniformity in particle size. The mean hydrodynamic diameters of the nanoparticles synthesized at 10, 20, 30, and 40 minutes are 314 nm, 266 nm, 250 nm, and 272 nm, respectively, as shown in Fig. S2a. Notably, the smallest hydrodynamic diameter is observed at the 30 minute synthesis time,

suggesting optimal conditions for particle size reduction during this time interval. However, the slight increase in size after 30 minutes suggests that, beyond this time, agglomeration of the particles occurs, leading to a larger particle size despite improved stability (with a higher zeta potential of 20.0 mV), as shown in Fig. S2b. This highlights the importance of fine-tuning synthesis times to achieve the desired nanoparticle size. The reduction in particle size observed for the 30 minute sample also ties into the UV-NIR absorbance spectra and optical bandgap findings.

The corresponding zeta potential values, depicted in Fig. S2b, are 5.3 mV, 10.7 mV, 9.6 mV, and 20.0 mV for the samples synthesized at 10, 20, 30, and 40 minutes, respectively. The zeta potential values above 10 mV for the sample synthesized at 40 minutes indicate improved colloidal stability, with the highest zeta potential of 20.0 mV observed, suggesting enhanced electrostatic repulsion between particles compared to other samples. However, it is evident that prolonged hydrothermal synthesis leads to limitations such as increased particle size and agglomeration, likely due to enhanced particle–particle interactions.[72] The observed variation in hydrodynamic diameter and zeta potential across the synthesis times reflects the influence of processing conditions on particle size and surface charge, both of which are critical parameters in determining the colloidal stability and dispersibility of the nanoparticles.

Assessment of structural features and size distribution of particles

The surface morphology of the BTNP samples was investigated using SEM analysis, as shown in Fig. 7. A clear variation in morphology is observed with the synthesis time. The samples prepared at 20 and 30 minutes exhibit uniformly distributed particles, with the 30 minute sample (Fig. 7c) exhibiting the most refined and homogeneous structure.

In contrast, the samples synthesized at 10 and 40 minutes (Fig. 7a and d) show evident particle aggregation. Using ImageJ software, the particle sizes were quantitatively analyzed, and the corresponding size distributions are shown as histograms in Fig. S3. The average particle sizes observed from the size distribution chart for the 10, 20, 30, and 40 minute samples were 89.75 nm, 63.44 nm, 51.55 nm, and 84.42 nm, respectively. Among these, the 30 minute sample demonstrated the smallest average size and the most uniform distribution, suggesting that this synthesis duration is optimal for producing particles with minimal size and high monodispersity. The uniformity in particle size observed under SEM mirrors the low polydispersity index (PDI) found in DLS

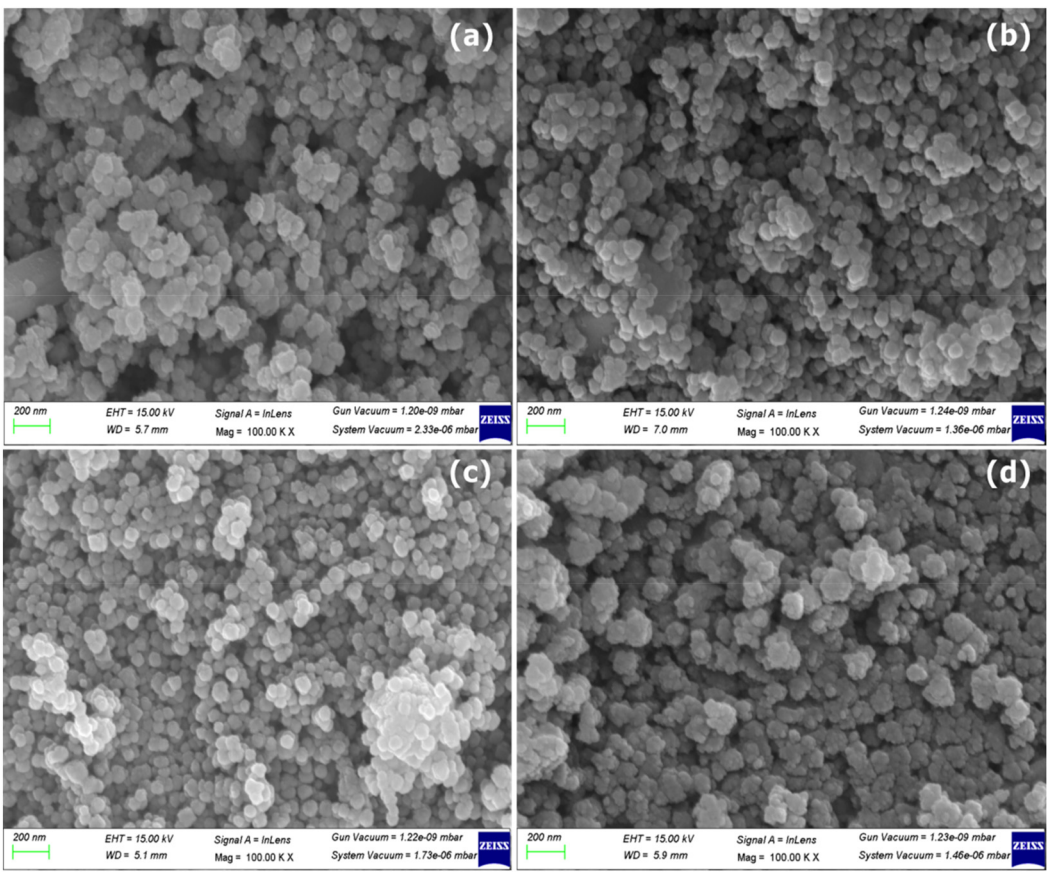

Fig. 7 SEM images of the fabricated nanomaterials at (a) 10 minutes, (b) 20 minutes, (c) 30 minutes, and (d) 40 minutes.

measurements, further confirming that 30 minutes is the optimal synthesis duration for the reduced particle size. Additionally, the moderately high zeta potential currently suggests good colloidal stability, preventing aggregation, which is reflected in the SEM results showing well-separated particles.

Evaluation of elemental distribution across the surface

Fig. 8 presents the EDX analysis for the BTNPs synthesized at different time intervals. The EDX spectra confirms the elemental composition of the samples, showing the presence of barium (Ba), titanium (Ti), and oxygen (O) across all synthesis durations, as depicted in Fig. 8(a–d).

The elemental composition varies with the synthesis time, with the most notable changes observed in the oxygen content. Specifically, the oxygen composition is notably lower in the nanoparticles synthesized for 30 minutes, which also exhibit the highest stability and crystallinity due to oxygen vacancies. This observation is consistent with the TGA results, which indicated a lower prevalence of oxygen-bound metal precursors in the 30 minute sample compared to the other samples. The lower oxygen content (atomic% = 19.78), as shown in Fig. 8c, at 30 minutes correlates with the improved structural order observed in the XRD results, highlighting that the optimal synthesis time not only achieves better crystallinity but also minimizes the presence of oxygen-related defects or residuals.

High-resolution imaging of internal lattice features

The highly refined nanostructure obtained after 30 minutes of synthesis was further characterized by HR-TEM, as shown in Fig. 9, to assess its crystallinity and internal lattice structure with high-resolution detail (Fig. 9a and b).

Fig. 9d presents the selected area electron diffraction (SAED) pattern, which reveals concentric polycrystalline diffraction rings corresponding to the interaction of the electron beam with the crystalline domains. The diffraction pattern is in excellent agreement with the characteristic cubic perovskite crystal structure of $BaTiO_3$, as corroborated by the XRD analysis. The first six diffraction rings are indexed to the (100), (110), (111), (200), (210), and (211) crystallographic planes, confirming the structural integrity of the material in the cubic phase.

Additionally, the HR-TEM image of an isolated $BaTiO_3$ nanocrystal, shown in Fig. 9c, provides a detailed view of the atomic arrangement. The presence of well-defined lattice fringes with an interplanar spacing of d_{110} = 0.239 nm substantiates the single-crystalline nature of the nanoparticles, demonstrating their high degree of crystallinity.

Analysis of surface-bound elements and their elemental states

The XPS survey spectrum confirmed the presence of barium (Ba), titanium (Ti), oxygen (O), and carbon (C) species (Fig. 10). To gain further insights into the electronic structure and oxidation states of the elements, the characteristic peaks corresponding to Ba 3d, O 1s, and Ti 2p were systematically deconvoluted and analysed. Baseline correction for all deconvoluted spectra was performed using OriginPro software, and the background was subtracted following the Tougaard method to ensure accurate peak fitting and interpretation.

The XPS spectra of Ba atoms for all the samples synthesized at varied time intervals are presented in Fig. 11(a–d). As shown in the figure, all BTNP samples exhibit two distinct Ba 3d spin–orbit states, where the peaks in the binding energy range of 777.0–780.0 eV correspond to Ba $3d_{5/2}$, while those between 793.5 and 795.5 eV correspond to Ba $3d_{3/2}$.[66]

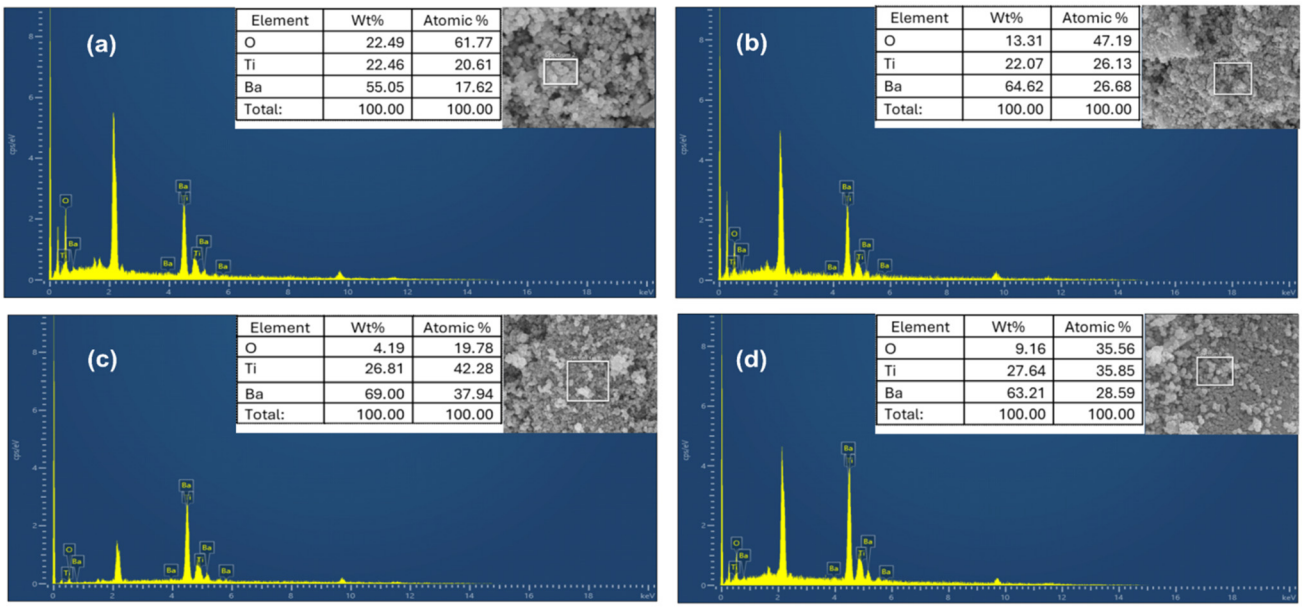

Fig. 8 EDX spectra of BTNPs synthesized at various time intervals: (a) 10 minutes, (b) 20 minutes, (c) 30 minutes, and (d) 40 minutes.

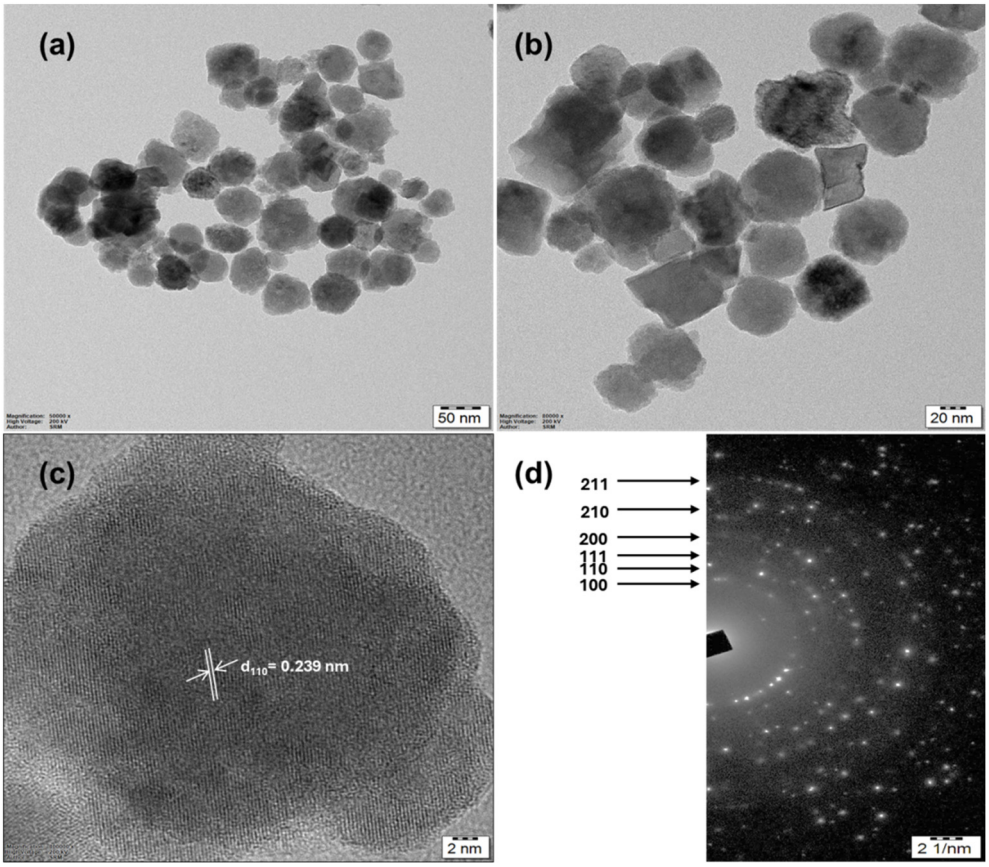

Fig. 9 TEM images of $BaTiO_3$ synthesized at 30 minutes. (a and b) TEM images at different magnifications; (c) HR-TEM image and (d) selected area electron diffraction (SAED) pattern.

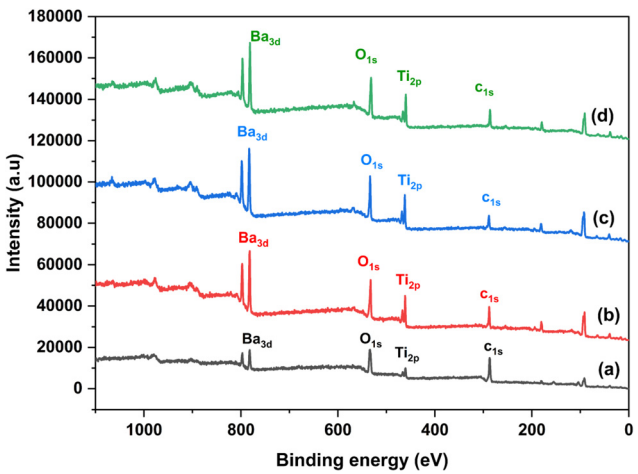

Fig. 10 XPS survey spectra of $BaTiO_3$ fabricated at (a) 10 minutes, (b) 20 minutes, (c) 30 minutes, and (d) 40 minutes.

From Fig. 11(a and d), the binding energy separation between Ba $3d_{5/2}$ and Ba $3d_{3/2}$ is found to be 15.3 eV,[73] which is consistent with the findings reported by Hudson *et al.*[74] In contrast, Fig. 11(b and c) reveal a splitting in both spin states, which implies that the peaks with higher intensities at the binding energies (778.2, 778.6 eV for Ba $3d_{5/2}$ and 793.5, 794.0 eV for Ba $3d_{3/2}$) are designated as Ba I, while the peaks with lower intensities at the binding energies (779.4, 780.0 eV for Ba $3d_{5/2}$ and 794.8, 795.5 eV for Ba $3d_{3/2}$) are labelled as Ba II.[57] The peaks at 778.6 and 794.0 eV can be attributed to point defects arising from barium vacancies.[75] The fitting parameters corresponding to all the peaks in Fig. 11 are summarized in Table 1.

Additionally, the binding energy difference between Ba I (Ba $3d_{5/2}$) and Ba I (Ba $3d_{3/2}$) is measured as 15.3 eV in Fig. 11b and 15.4 eV in Fig. 11c. These values correspond to $BaTiO_3$, confirming the formation of the perovskite phase. The Ba I and Ba II species are attributed to BaO and BaO_2, respectively, both of which exist in the Ba^{2+} oxidation state.[76–78] The oxidation state of oxygen (O) is −2 in BaO and −1 in BaO_2.[79] In the BaO phase, barium typically exhibits a six-coordinate environment, forming an octahedral arrangement with six oxygen atoms. In the BaO_2 phase, barium is seven-coordinate, adopting a distorted pentagonal bipyramidal geometry with oxygen atoms. Additionally, the oxygen in BaO_2 exists as O_2 dumbbells, rather than individual oxygen atoms as in BaO.[80] Surface oxidation of $BaTiO_3$, resulting in the formation of BaO_2 like species, can substantially modify its surface chemistry, thereby influencing its electrical, optical, and catalytic

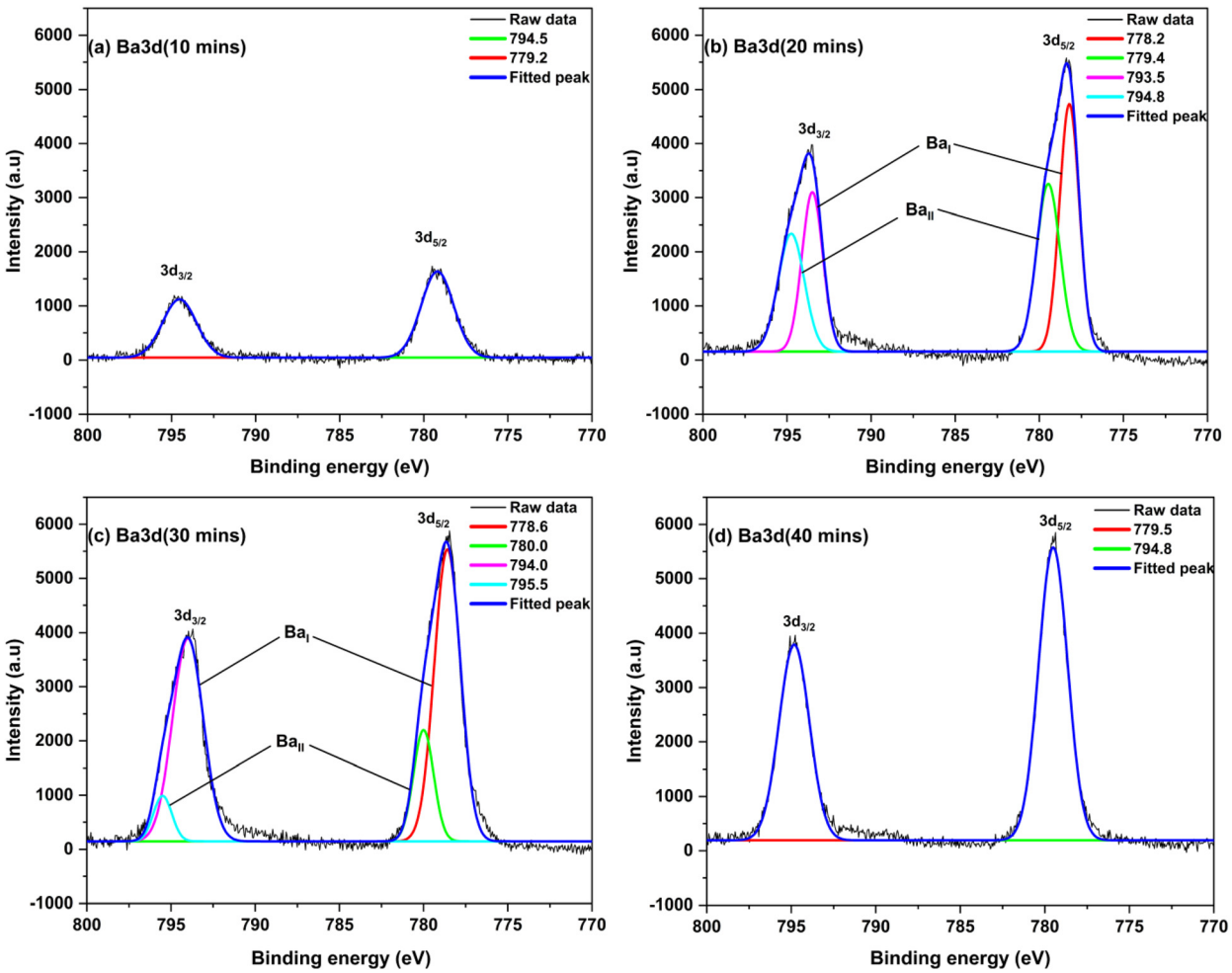

Fig. 11 Deconvoluted spectra of Ba 3d of $BaTiO_3$ fabricated at (a) 10 minutes, (b) 20 minutes, (c) 30 minutes, and (d) 40 minutes.

Table 1 Fitting parameters of Ba 3d XPS spectra for the BTNPs synthesized under varying reaction time conditions

Samples fabricated at different time intervals	Ba 3d		Binding energy (eV)	Area	FWHM (eV)
10 min	3d5/2	—	779.2	3847.99	2.27
	3d3/2	—	794.5	2691.06	2.35
20 min	3d5/2	BaO	778.2	6704.32	1.38
		BaO_2	779.5	5440.79	1.65
	3d3/2	BaO	793.5	4582.49	1.46
		BaO_2	794.8	4257.07	1.83
30 min	3d5/2	BaO	778.6	10 523.02	1.83
		BaO_2	780.0	3084.90	1.41
	3d3/2	BaO	794.0	8586.27	2.15
		BaO_2	795.5	1162.83	1.30
40 min	3d5/2	—	779.5	11 520.04	2.01
	3d3/2	—	794.8	8101.78	2.11

properties. This transformation is frequently observed at the surface due to the thermodynamic instability of $BaTiO_3$ under specific environmental conditions, which promotes the leaching of Ba^{2+} ions and the development of a titanium-enriched surface layer.[81–83]

The deconvoluted XPS spectra of oxygen atoms in the BTNP samples corresponding to various reaction times are presented in Fig. 12(a–d). The O 1s XPS spectra of all the samples are shown in Fig. 12, which exhibit multiple peaks corresponding to different oxygen species. A literature survey suggests that the binding energy of oxygen varies depending on its chemical environment. Specifically, the peaks observed in the binding energy range of 528.8–530.0 eV correspond to lattice oxygen (O^{2-}), which is associated with the Ti–O bonds in $BaTiO_3$. The peaks appearing between 530.0 and 531.5 eV are attributed to ionized oxygen vacancies or defects, while those in the range of 531.5–532.5 eV correspond to adsorbed oxygen species, including carbonates, hydroxyl groups, or water molecules.[84–86]

A comparative analysis of the spectra in Fig. 12(a–d) indicates that BTNPs synthesized at 30 minutes (Fig. 12c) exhibit enhanced crystallinity, with the supporting area values presented in Table 2, which are characterized by an increased proportion of lattice oxygen and a reduction in adsorbed oxygen and oxygen defects. This observation aligns with the EDX analysis, which shows a relative decrease in the oxygen content at this synthesis duration. The fitting parameters for Fig. 12(a–d) are provided in Table 2.

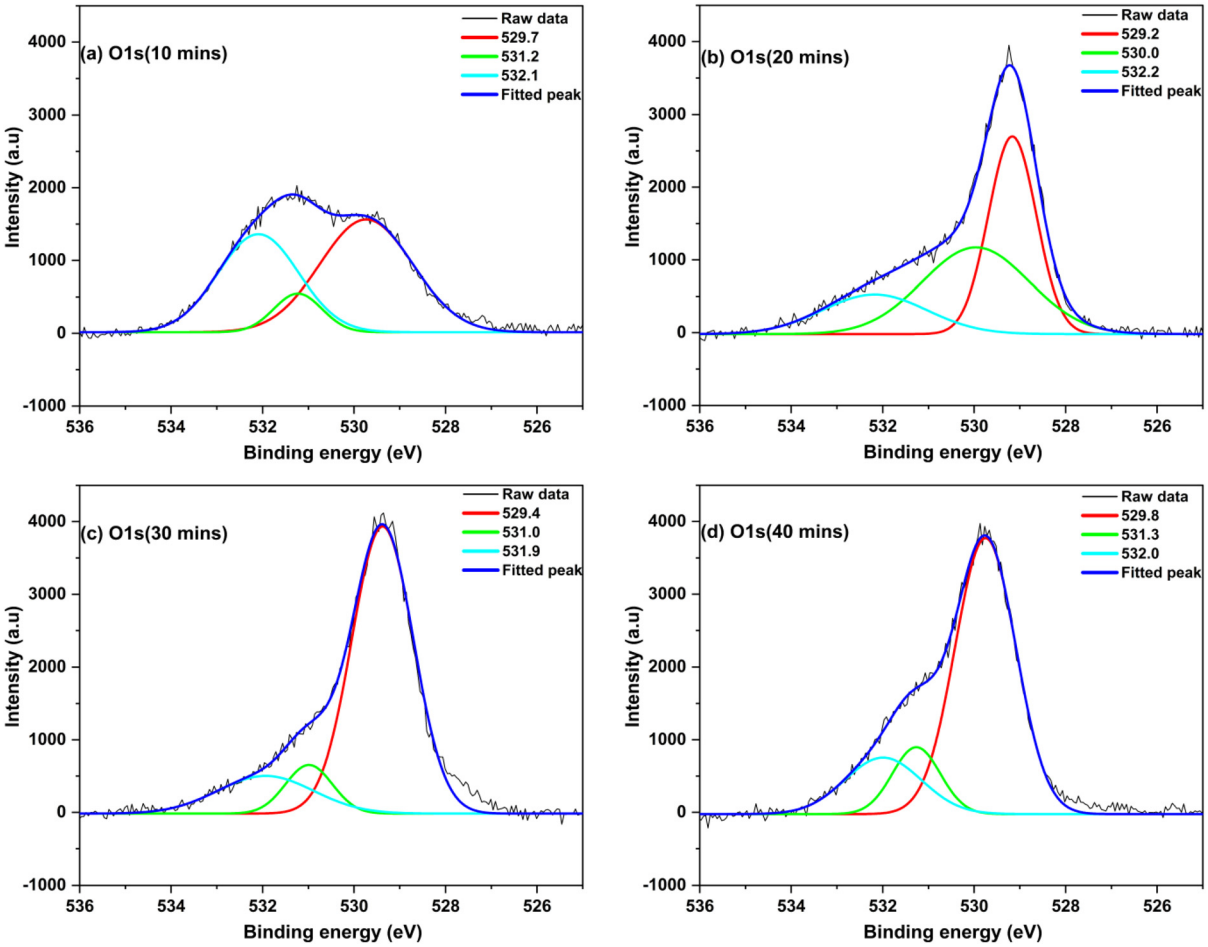

Fig. 12 Deconvoluted XPS spectra of O 1s of $BaTiO_3$ fabricated at (a) 10 minutes, (b) 20 minutes, (c) 30 minutes, and (d) 40 minutes.

Table 2 Fitting parameters of O 1s XPS spectra for $BaTiO_3$ formed at distinct time intervals

Samples fabricated at different time intervals	O 1s	Binding energy (eV)	Area	FWHM (eV)
10 min	Lattice oxygen	529.7	3925.37	2.38
	Oxygen defect	531.2	699.81	1.24
	Adsorbed oxygen	532.1	2965.76	2.07
20 min	Lattice oxygen	529.2	3556.66	1.23
	Oxygen defect	530.0	3480.22	2.75
	Adsorbed oxygen	532.2	1556.07	2.69
30 min	Lattice oxygen	529.4	6664.86	1.58
	Oxygen defect	531.0	858.94	1.21
	Adsorbed oxygen	531.9	1363.57	2.47
40 min	Lattice oxygen	529.8	6317.09	1.56
	Oxygen defect	531.3	1208.36	1.23
	Adsorbed oxygen	532.0	1628.43	1.97

Furthermore, the presence of a higher concentration of lattice oxygen in BTNPs synthesized at 30 minutes is corroborated by the area under the curve in Table 2, which shows a significant increase compared to other synthesis durations.

The high-resolution XPS spectra of the Ti 2p region, after deconvolution, are presented in Fig. 13(a–d). All samples exhibit two primary peaks, which correspond to the spin–orbit splitting of Ti $2p_{3/2}$ and Ti $2p_{1/2}$, appearing within the binding energy ranges of 457.7–458.1 eV and 463.4–463.7 eV, respectively.

These binding energy values agree with previously reported XPS data for Ti^{4+}, confirming the oxidation state of titanium in the samples.[87–90] The fitting parameters for all peaks observed in Fig. 13 are detailed in Table 3. Together, the high-resolution XPS analysis of Ba, O, and Ti confirms the formation of a phase-pure $BaTiO_3$ perovskite structure at 30 minutes of synthesis, with reduced surface defects and enhanced lattice oxygen incorporation which together signify improved crystallinity and chemical homogeneity.

Probing interfacial electron transfer kinetics through cyclic voltammetry

Fig. 14a presents the CV curves of bare ITO and ITO modified BTNPs-20 minutes and BTNPs-30 minutes, each exhibiting a duck-shaped CV curve with varying redox peak currents. The

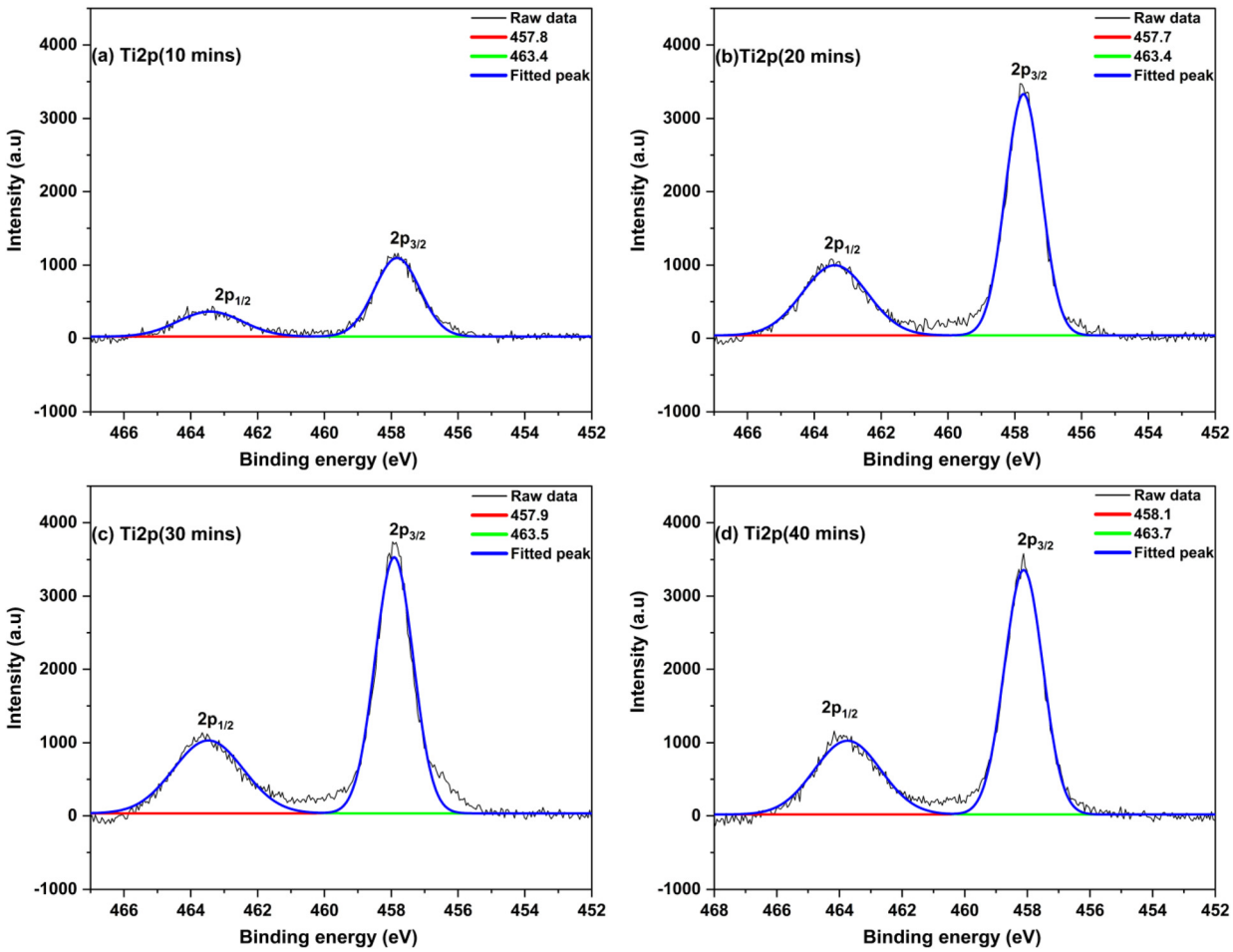

Fig. 13 Deconvoluted XPS spectra of Ti 2p of $BaTiO_3$ fabricated at (a) 10 minutes, (b) 20 minutes, (c) 30 minutes, and (d) 40 minutes.

Table 3 Fitting parameter of Ti 2p XPS spectra for the $BaTiO_3$ synthesis conducted for different time durations

Samples fabricated at different time intervals	Ti 2p	Binding energy (eV)	Area	FWHM (eV)
10 min	2p3/2	457.8	1826.38	1.60
	2p1/2	463.4	829.23	2.28
20 min	2p3/2	457.7	4432.26	1.26
	2p1/2	463.4	2339.65	2.29
30 min	2p3/2	457.9	5000.12	1.34
	2p1/2	463.5	2615.71	2.47
40 min	2p3/2	458.1	5135.30	1.45
	2p1/2	463.7	2679.43	2.50

modification of ITO with BTNPs-20 and BTNPs-30 demonstrated higher peak current, highlighting enhanced interfacial electron transfer kinetics. Specifically, BTNPs-30/ITO revealed a higher anodic peak current (I_{pa}) of 587 μA, compared to BTNPs-20/ITO which exhibited an I_{pa} of 534 μA, indicating higher conductivity and electrocatalytic properties of BTNPs-30.[91] Such enhancement can be ascribed to improved crystallinity, smaller particle size and homogeneous morphology which enables rapid electron transfer at the interface.[16] In contrast, the partial aggregation of BTNPs, as seen in Fig. 7b (BTNPs-20), restricts electron transfer, leading to a reduced I_{pa}.

We further conducted CV at distinct scan rates to examine the electron transfer kinetics at the BTNPs-30/ITO–electrolyte interface. As depicted in Fig. 14b, increasing the potential scan rate from 0.01 to 0.1 V s^{-1} resulted in an increase in redox peak currents (I_{pa} and I_{pc}), consistent with the Randle–Sevcik equation given below.

$$I_p = (2.69 \times 10^5) n^{3/2} A D^{1/2} C v^{1/2}$$

where n refers to the number of electrons involved in the redox process (for $Fe(CN)_6^{3-/4-}$, $n = 1$), D is the diffusion coefficient of the electroactive species in $cm^2\ s^{-1}$, C is the concentration of the electroactive species in mol cm^{-3} (5 mM of ferricyanide), v is the scan rate in V s^{-1}, and A is the electroactive surface area in cm^2 (here $A = 1\ cm^2$). As illustrated in Fig. 14c, linear dependence of I_{pa} and cathodic peak current (I_{pc}) on the square root of the scan rate with a linear regression equation of $I_{pa} = 0.00255v^{1/2} + 1.83 \times 10^{-5}$ (I_{pa} in A, v in V s^{-1}; $R^2 = 0.994$) and $I_{pc} = -0.00188v^{1/2} - 1.49 \times 10^{-4}$ (I_{pc} in A, v in V s^{-1};

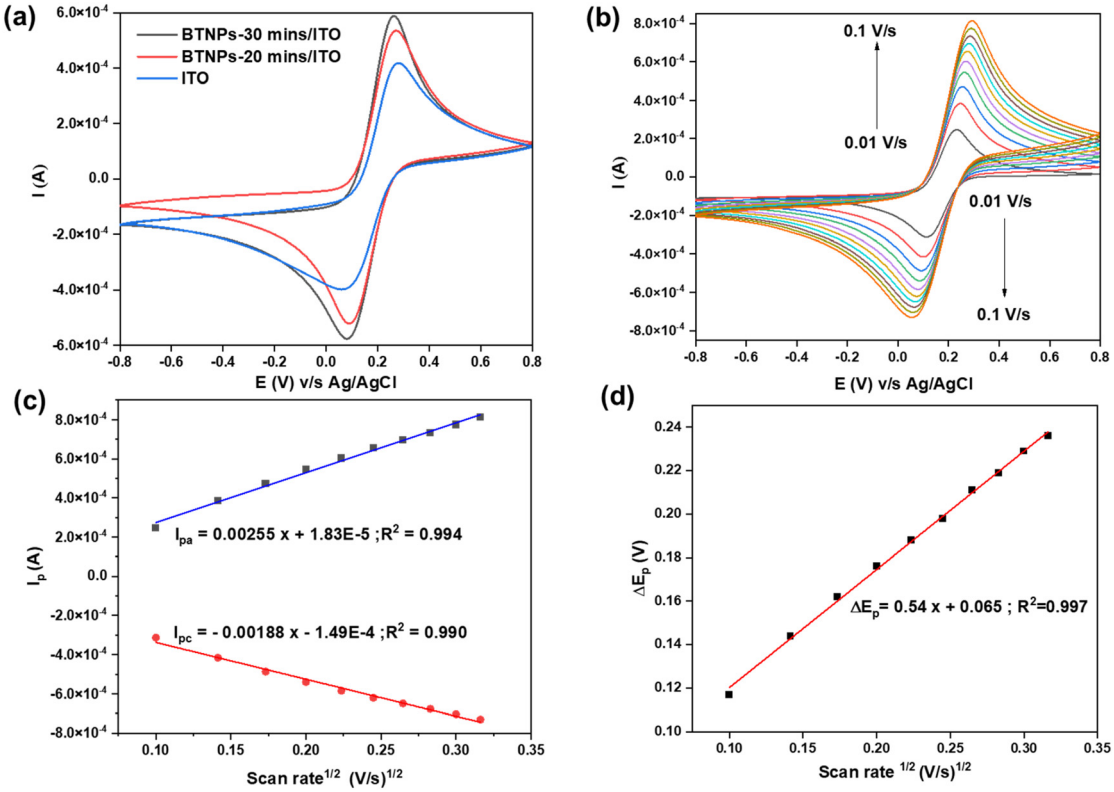

Fig. 14 (a) CV curves of bare ITO, BTNPs-20/ITO and BTNPs-30/ITO. (b) CV curves of BTNPs-30/ITO at different scan rates. (c) Anodic and cathodic peak current dependence on the square root of the scan rate. (d) Variation of peak-to-peak separation potential with respect to the square root of the scan rate.

R^2 = 0.990) affirms diffusion controlled reaction kinetics at the interface.[92] The peak–peak separation potential (ΔE_p) also exhibited linear dependence on the $v^{1/2}$, as shown in Fig. 14d, with a linear regression equation of $\Delta E_p = 0.54v^{1/2} + 0.065$ (ΔE_p in V, v in V s^{-1}; R^2 = 0.997), indicating quasi-reversible characteristics of BTNPS-30/ITO. The anodic to cathodic peak current ratio (I_{pa}/I_{pc}) of 1.01 marginally higher than unity further validates the quasi-reversibility of electron transfer kinetics at the BTNPs-30/ITO–electrolyte interface.[93]

Discussion

The systematic characterization of BTNPs synthesized *via* the microwave solvothermal method at various time intervals provides valuable insights into the effects of the synthesis time on their structural, optical, surface, and compositional attributes. XRD analysis confirms that the synthesized BTNPs predominantly crystallize in the cubic phase, with no evidence of the tetragonal phase, as indicated by the absence of peak splitting at $2\theta = 45°$. The increased peak intensity and sharpness for the sample synthesized for 30 minutes point to improved crystallinity, reduced defect density and larger coherent scattering domains. This finding is corroborated by the TGA results, where the 30 minute sample exhibits the lowest total weight loss, indicating more complete crystallization and higher phase purity and fewer residual organics. Together, the XRD and TGA results together demonstrate that extending the synthesis time to 30 minutes optimizes the crystallinity of the nanoparticles, which is critical for achieving crystallographically ordered and thermally stable BTNPs. FTIR spectra confirms the perovskite structure of $BaTiO_3$ and reveals the presence of surface-bound functional groups, such as OH^- and carboxylate residues, more prominent in shorter-duration samples. The lower oxygen content observed in the 30 minute sample, as confirmed by EDX analysis, aligns with the TGA findings of reduced hydroxyl groups. This reduction in oxygen content is associated with diminished surface hydroxylation and improved lattice ordering, supporting the XRD and TGA observations.

UV-NIR absorption spectroscopy indicates that the optical bandgap energy decreases with increased synthesis time up to 30 minutes, reflecting a reduction in particle size and enhanced crystallinity. Beyond 30 minutes, a slight bandgap widening is observed, possibly due to particle agglomeration or growth. These findings are consistent with the DLS data, which show the smallest hydrodynamic diameter for the 30 minute sample, indicating a critical threshold for particle

size reduction. The observed optical bandgap behavior elucidates the importance of the synthesis time duration on the electronic properties.

SEM analysis revealed that the BTNPs synthesized at 30 minutes exhibited a well-defined morphology with a uniform and narrow particle size distribution. This observation is consistent with DLS measurements, which showed the smallest hydrodynamic diameter at this time point. Notably, the particle size remained minimized at 30 minutes but increased beyond this duration, likely due to the onset of particle agglomeration or growth. This trend is corroborated by crystallite size estimations from the XRD data using the Scherrer equation, which also indicated the smallest crystallite dimensions at 30 minutes, further supporting the observed size evolution. In contrast, the samples synthesized at 10 and 40 minutes showed significant particle aggregation in SEM images, reflecting poorer control over particle dispersion and size uniformity. These findings are additionally supported by zeta potential measurements, where the 30 minute sample exhibited moderate colloidal stability, limiting particle–particle interactions and thereby preserving uniform dispersion.

Raman spectroscopy provided valuable insights into the vibrational behavior of the TiO_6 octahedral units and the structural characteristics of the BTNPs. The presence of broad Raman peaks and subtle shifts in the vibrational modes, particularly those associated with Ti–O bonds, indicates local distortions within the crystal lattice and suggests partial structural disorder or a coexistence of cubic and tetragonal phases. This interpretation is further supported by ATR-FTIR spectra, where the Ti–O stretching vibrations observed in the 510–550 cm^{-1} is a common region that similarly points to both cubic and tetragonal environments. HR-TEM (Fig. 9b) also revealed particles with sharp edge corners and curved corners, indicating a mixture of cubic and tetragonal phases, although the cubic phase remains predominant. These observations are in good agreement with XRD analysis, which confirmed the overall dominance of the cubic perovskite phase based on the absence of peak splitting at $2\theta \approx 45°$, while still allowing for the presence of minor structural distortions.

TEM, supported by selected area electron diffraction (SAED), offers critical insights into the microstructural features of BTNPs synthesized under optimized conditions. The HR-TEM images reveal well-defined nanoscale morphology with uniform particle shapes and exhibit distinct lattice fringes, indicative of high crystallinity and well-ordered atomic arrangements. The corresponding SAED patterns exhibit sharp, concentric diffraction rings that can be indexed to the (100), (110), (111), (200), (210), and (211) planes of $BaTiO_3$, confirming the polycrystalline nature of the material. These diffraction features are in excellent agreement with the XRD results, both of which confirm that the synthesized BTNPs predominantly crystallize in the cubic perovskite phase. The congruence between the SAED and XRD patterns strongly validates the structural integrity and phase purity of the material under the 30 minute synthesis conditions.

Table 4 Comparison of the traditional hydrothermal method and the microwave-assisted solvothermal method

Properties	Traditional hydrothermal synthesis	Microwave-assisted synthesis
Reaction time	24 hours (ref. 94) and 7 hours (ref. 95)	30 minutes
Morphology	Cubic (ref. 94 and 95)	Cubic
Temperature	180 °C (ref. 94 and 95)	180 °C
Particle size	40 nm (ref. 94) and 52 nm (ref. 95)	51.6 nm

XPS analysis confirms the successful synthesis of BTNPs, as evidenced by the presence of characteristic binding energy peaks corresponding to Ba^{2+}, Ti^{4+}, and various oxygen species. The observed oxygen states, including lattice oxygen, ionized oxygen vacancies, and adsorbed oxygen species, indicate variations in the structural and electronic properties of the synthesized BTNPs. Among the different synthesis durations, the 30 minute synthesized BTNPs exhibit the highest crystallinity, as reflected in the increased proportion of lattice oxygen (Ti–O bonds) and reduced adsorbed oxygen and ionized oxygen vacancies. This finding aligns well with the EDX analysis, which indicates a reduction in the excess oxygen content, which also aligns with the TGA results, which suggests improved thermal stability for the sample synthesized at 30 minutes.

As a result of CV analysis, BTNPs synthesized at 30 minutes exhibited superior electrocatalytic properties. The enhanced crystallinity and structural homogeneity reduced the density of trap states, thereby facilitating an efficient charge transport at the BTNPs/ITO–electrolyte interface. Such improvements are crucial and position BTNPs synthesized at 30 minutes as a promising electroactive interface that can be further explored for optoelectronic and electroanalytical applications. The combined results further support the optimized synthesis conditions at 30 minutes, leading to more stoichiometric and structurally stable BTNPs.

A comparison between the conventional hydrothermal method and the microwave-assisted approach for the synthesis of $BaTiO_3$ using identical precursors demonstrates that the microwave-assisted solvothermal method offers significant advantages in terms of reaction kinetics, particle uniformity, and agglomeration control. Microwave irradiation enables rapid and homogeneous volumetric heating, which accelerates nucleation and reduces the reaction time from several hours (7–24 h) to just 30 minutes. This rapid heating promotes uniform supersaturation and limits secondary growth, yielding cubic BTNPs with improved morphological homogeneity and reduced agglomeration compared to those synthesized *via* conventional hydrothermal methods. A detailed comparative analysis of BTNPs synthesized by both methods is presented in Table 4.[94,95]

Conclusion

The monodisperse nanostructured $BaTiO_3$ was synthesized using a microwave-assisted solvothermal method. Various

techniques were employed to characterize the prepared particles and determine the optimal reaction time for producing fine, monodisperse nanoparticles. XRD and SEM analyses revealed that ultrafine cubic-structured nanoparticles, with a size of approximately 50 nm, were obtained at 180 °C with a reaction time of 30 minutes. The particles synthesized under these conditions exhibited thermal stability and contained fewer impurities compared to the samples produced at other time intervals. This time-dependent synthesis of perovskite BTNPs using microwave-assisted solvothermal techniques provides valuable insights into the morphological characteristics of nanomaterials. Additionally, the synthesized BTNPs enabled tuning of the optical bandgap with respect to the synthesis time. Electrochemical studies demonstrate enhanced interfacial electron transfer kinetics, ascribed to superior structural and morphological properties achieved at the optimized synthesis time. The tunability of the optical bandgap and electrocatalytic properties highlights microwave-assisted synthesis as a reliable strategy to obtain BTNPs tailored for optoelectronic and electroanalytical applications. Further studies on dielectric properties were conducted to evaluate the potential for biomedical applications.

Conflicts of interest

The authors declare that they have no competing interests.

Data availability

The data supporting the findings of this study are provided in the supplementary information (SI). Supplementary information is available. See DOI: https://doi.org/10.1039/d5nr03238e.

Additional datasets related to this work are available from the corresponding author upon reasonable request.

Acknowledgements

This research was supported by the RSL Fellowship, the Department of Biotechnology (CHE2122003DOBIUDAY), and the Ministry of Education (MoE) (Faculty Initiation Grant, IIT Tirupati), Government of India. Vinith Johnson extends his gratitude to the PMRF fellowship (PMRF ID: 3203668) for the research grant as well as fellowship assistance and to the MoE, Government of India for the fellowship assistance. The authors would also like to thank the Department of Chemical Engineering and the Department of Chemistry, IIT Tirupati, and the Institute Instrumentation Centre, the Department of Biosciences and Bioengineering, and the Centre for Nanotechnology, IIT Roorkee, for providing various characterization facilities.

References

1 S.-O. Kang, B. H. Park and Y.-I. Kim, Growth Mechanism of Shape-Controlled Barium Titanate Nanostructures through Soft Chemical Reaction, *Cryst. Growth Des.*, 2008, **8**(9), 3180–3186.
2 R. Asiaie, W. Zhu, S. A. Akbar and P. K. Dutta, Characterization of Submicron Particles of Tetragonal $BaTiO_3$, *Chem. Mater.*, 1996, **8**(1), 226–234.
3 M. H. Frey and D. A. Payne, Grain-size effect on structure and phase transformations for barium titanate, *Phys. Rev. B: Condens. Matter Mater. Phys.*, 1996, **54**(5), 3158–3168.
4 P. Perriat, J. Niepce and G. Caboche, Thermodynamic considerations of the grain size dependency of material properties: A new approach to explain the variation of the dielectric permittivity of $BaTiO_3$ with grain size, *J. Therm. Anal. Calorim.*, 1994, **41**(2–3), 635–649.
5 L. Xu, K. Zhu, J. Wang, Q. Gu, Y. Cao, H. Zheng, *et al.*, Microwave-assisted sol–hydrothermal synthesis of tetragonal barium titanate nanoparticles with hollow morphologies, *J. Mater. Sci.: Mater. Electron.*, 2015, **26**(3), 1597–1601.
6 A. Rached, M. A. Wederni, K. Khirouni, S. Alaya, R. J. Martín-Palma and J. Dhahri, Structural, optical and electrical properties of barium titanate, *Mater. Chem. Phys.*, 2021, **267**, 124600.
7 P.-J. Chang, M.-S. Chen, C.-H. Cheng, Y.-J. Chiou, C.-Y. Chen, C.-Y. Su, *et al.*, Effects of Calcination Temperature on the Synthesis of One-Pot Sol-Gelled Barium Titanate Powder and Its Performance as an Endodontic Radiopacifier, *Materials*, 2024, **17**(11), 2701.
8 J. Čulić-Viskota, W. P. Dempsey, S. E. Fraser and P. Pantazis, Surface functionalization of barium titanate SHG nanoprobes for in vivo imaging in zebrafish, *Nat. Protoc.*, 2012, **7**(9), 1618–1633.
9 F. Madzharova, Á. Nodar, V. Živanović, M. R. S. Huang, C. T. Koch, R. Esteban, *et al.*, Gold- and Silver-Coated Barium Titanate Nanocomposites as Probes for Two-Photon Multimodal Microspectroscopy, *Adv. Funct. Mater.*, 2019, **29**(49), 1904289.
10 T. Jordan, M. A. O'Brien, C.-P. Spatarelu and G. P. Luke, Antibody-Conjugated Barium Titanate Nanoparticles for Cell-Specific Targeting, *ACS Appl. Nano Mater.*, 2020, **3**(3), 2636–2646.
11 G. Ciofani, S. Danti, D. D'Alessandro, S. Moscato, M. Petrini and A. Menciassi, Barium Titanate Nanoparticles: Highly Cytocompatible Dispersions in Glycol-chitosan and Doxorubicin Complexes for Cancer Therapy, *Nanoscale Res. Lett.*, 2010, **5**(7), 1093.
12 T. Hoshina, S. Wada, Y. Kuroiwa and T. Tsurumi, Composite structure and size effect of barium titanate nanoparticles, *Appl. Phys. Lett.*, 2008, **93**(19), 192914.
13 G. Ciofani, S. Danti, D. D'Alessandro, L. Ricotti, S. Moscato, G. Bertoni, *et al.*, Enhancement of Neurite Outgrowth in Neuronal-Like Cells following Boron Nitride Nanotube-Mediated Stimulation, *ACS Nano*, 2010, **4**(10), 6267–6277.

14 A. H. Rajabi, M. Jaffe and T. L. Arinzeh, Piezoelectric materials for tissue regeneration: A review, *Acta Biomater.*, 2015, **24**, 12–23.
15 R. H. Huang, N. B. Sobol, A. Younes, T. Mamun, J. S. Lewis, R. V. Ulijn, *et al.*, Comparison of Methods for Surface Modification of Barium Titanate Nanoparticles for Aqueous Dispersibility: Toward Biomedical Utilization of Perovskite Oxides, *ACS Appl. Mater. Interfaces*, 2020, **12**(46), 51135–51147.
16 B. Arumugam, V. Nagarajan, J. Annaraj and S. K. Ramaraj, Barium titanate nanoparticle-based disposable sensor for nanomolar level detection of the haematotoxic pollutant quinol in aquatic systems, *New J. Chem.*, 2022, **46**(6), 3006–3016.
17 M. Ali, S. Sharma, R. Singh, K. Sharma, S. Majhi, D. Guin, *et al.*, Barium Titanate Nanocubes as a Dual Electrochemical Sensor for Detection of Dopamine and Acetaminophen, *J. Electrochem. Soc.*, 2022, **169**(6), 067512.
18 Y. Zhu, B. Ma, K. Wang, Z. Sun, K. Ren and Y. Wang, Electric field-assisted solid-state reaction of $BaCO_3$-TiO_2 system, *J. Am. Ceram. Soc.*, 2021, **104**(12), 6572–6578.
19 S. Kudłacik-Kramarczyk, A. Drabczyk, M. Głąb, P. Dulian, R. Bogucki, K. Miernik, *et al.*, Mechanochemical Synthesis of $BaTiO_3$ Powders and Evaluation of Their Acrylic Dispersions, *Materials*, 2020, **13**(15), 3275.
20 S.-G. Kwon, B.-H. Park, K. Choi, E.-S. Choi, S. Nam, J.-W. Kim, *et al.*, Solvothermally synthesized tetragonal barium titanate powders using H_2O/EtOH solvent, *J. Eur. Ceram. Soc.*, 2006, **26**(8), 1401–1404.
21 H. Xu, L. Gao and J. Guo, Preparation and characterizations of tetragonal barium titanate powders by hydrothermal method, *J. Eur. Ceram. Soc.*, 2002, **22**(7), 1163–1170.
22 H. Xu and L. Gao, Tetragonal Nanocrystalline Barium Titanate Powder: Preparation, Characterization, and Dielectric Properties, *J. Am. Ceram. Soc.*, 2003, **86**(1), 203–205.
23 K.-Y. Chen and Y.-W. Chen, Preparation of barium titanate ultrafine particles from rutile titania by a hydrothermal conversion, *Powder Technol.*, 2004, **141**(1), 69–74.
24 W. Sun, W. Liu and J. Li, Effects of chloride ions on hydrothermal synthesis of tetragonal $BaTiO_3$ by microwave heating and conventional heating, *Powder Technol.*, 2006, **166**(2), 55–59.
25 H. Zheng, K. Zhu, Q. Wu, J. Liu and J. Qiu, Preparation and characterization of monodispersed $BaTiO_3$ nanocrystals by sol–hydrothemal method, *J. Cryst. Growth*, 2013, **363**, 300–307.
26 R. N. Viswanath and S. Ramasamy, Preparation and ferroelectric phase transition studies of nanocrystalline $BaTiO_3$, *Nanostruct. Mater.*, 1997, **8**(2), 155–162.
27 R. Kavian and A. Saidi, Sol–gel derived $BaTiO_3$ nanopowders, *J. Alloys Compd.*, 2009, **468**(1), 528–532.
28 S. Kim, M. Lee, T. Noh and C. Lee, Preparation of barium titanate by homogeneous precipitation, *J. Mater. Sci.*, 1996, **31**(14), 3643–3645.
29 A.-h. Shi, W.-b. Yan, Y.-j. Li and K.-l. Huang, Preparation and characterization of nanometer-sized barium titanate powder by complex-precursor method, *J. Cent. South Univ. Technol.*, 2008, **15**(3), 334–338.
30 W.-S. Jung, J. Park, Y. Park and D.-H. Yoon, Effects of impurities on the properties of $BaTiO_3$ synthesized from barium titanyl oxalate, *Ceram. Int.*, 2010, **36**(6), 1997–2002.
31 W. Maison, R. Kleeberg, R. B. Heimann and S. Phanichphant, Phase content, tetragonality, and crystallite size of nanoscaled barium titanate synthesized by the catecholate process: effect of calcination temperature, *J. Eur. Ceram. Soc.*, 2003, **23**(1), 127–132.
32 O. Okhay and A. Tkach, Current Achievements in Flexible Piezoelectric Nanogenerators Based on Barium Titanate, *Nanomaterials*, 2023, **13**(6), 988.
33 M. Thamima, Y. Andou and S. Karuppuchamy, Microwave assisted synthesis of perovskite structured $BaTiO_3$ nanospheres via peroxo route for photocatalytic applications, *Ceram. Int.*, 2017, **43**(1, Part A), 556–563.
34 C. Chang, S. Rad, L. Gan, Z. Li, J. Dai and A. Shahab, Review of the sol–gel method in preparing nano TiO_2 for advanced oxidation process, *Nanotechnol. Rev.*, 2023, **12**(1), 20230150.
35 W. Bahloul, O. Oddes, V. Bounor-Legaré, F. Mélis, P. Cassagnau and B. Vergnes, Reactive extrusion processing of polypropylene/TiO_2 nanocomposites by in situ synthesis of the nanofillers: Experiments and modeling, *AIChE J.*, 2011, **57**(8), 2174–2184.
36 D. Masekela, N. C. Hintsho-Mbita, B. Ntsendwana and N. Mabuba, Thin Films (FTO/$BaTiO_3$/AgNPs) for Enhanced Piezo-Photocatalytic Degradation of Methylene Blue and Ciprofloxacin in Wastewater, *ACS Omega*, 2022, **7**(28), 24329–24343.
37 E. Chávez, S. Fuentes, R. A. Zarate and L. Padilla-Campos, Structural analysis of nanocrystalline $BaTiO_3$, *J. Mol. Struct.*, 2010, **984**(1), 131–136.
38 M. D. Toomey, K. Gao, G. P. Mendis, E. B. Slamovich and J. A. Howarter, Hydrothermal Synthesis and Processing of Barium Titanate Nanoparticles Embedded in Polymer Films, *ACS Appl. Mater. Interfaces*, 2015, **7**(51), 28640–28646.
39 Y. Mao, S. Mao, Z.-G. Ye, Z. Xie and L. Zheng, Solvothermal synthesis and Curie temperature of monodispersed barium titanate nanoparticles, *Mater. Chem. Phys.*, 2010, **124**(2), 1232–1238.
40 A. F. Suzana, S. Liu, J. Diao, L. Wu, T. A. Assefa, M. Abeykoon, *et al.*, Structural Explanation of the Dielectric Enhancement of Barium Titanate Nanoparticles Grown under Hydrothermal Conditions, *Adv. Funct. Mater.*, 2023, **33**(19), 2208012.
41 M. Singh, B. C. Yadav, A. Ranjan, M. Kaur and S. K. Gupta, Synthesis and characterization of perovskite barium titanate thin film and its application as LPG sensor, *Sens. Actuators, B*, 2017, **241**, 1170–1178.
42 M. Fakhar-e-Alam, S. Saddique, N. Hossain, A. Shahzad, I. Ullah, A. Sohail, *et al.*, Synthesis, Characterization, and Application of $BaTiO_3$ Nanoparticles for Anti-Cancer Activity, *J. Cluster Sci.*, 2023, **34**(4), 1745–1755.

43 G. S. Jassim, M. Najim and W. Salih, Preparation of Micro Barium Titanate Powder and Comparison with Nano Powder Properties, *J. Appl. Sci. Nanotechnol.*, 2021, **1**(4), 12–23.

44 M. López, G. Fourlaris, B. Rand and F. L. Riley, Characterization of Barium Titanate Powders: Barium Carbonate Identification, *J. Am. Ceram. Soc.*, 1999, **82**(7), 1777–1786.

45 M. Bakhtbidar, I. Amaechi, A. Dörfler, A. Merlen and A. Ruediger, Direct Observation of Carbonate Chemisorption on Barium Titanate Surfaces by Tip-Enhanced Raman Spectroscopy, *Adv. Mater. Interfaces*, 2024, **11**(15), 2300993.

46 A. Y. Al-Ahmad, Preparation and study of microstructures, optical properties and oscillator parameters of titanium(IV) oxide (TiO_2) film, *Opt. Spectrosc.*, 2012, **113**(2), 197–203.

47 A. Saka, L. T. Jule, B. Badassa, L. Gudata, N. Nagaprasad, R. Shanmugam, *et al.*, Biosynthesis of TiO_2 nano particles by using Rosemary (Rosmarinus officinalis) leaf extracts and its application for crystal dye degradation under sunlight, *BMC Chem.*, 2024, **18**(1), 123.

48 H. Almaghamsi, Structural, optical, and morphological properties of PVC-$BaTiO_3$ nanocomposite films, *J. Mol. Liq.*, 2024, **412**, 125826.

49 A. A. Gadgeel, S. T. Mhaske, C. Duerr and K. L. Liu, *In situ* Preparation and Characterization of Aconitic Acid Capped Fe_3O_4 Nanoparticle by Using Citric Acid as a Reducing Agent, *J. Inorg. Organomet. Polym. Mater.*, 2019, **29**(5), 1688–1700.

50 M. K. Trivedi, G. Nayak, S. Patil, R. M. Tallapragada, O. Latiyal and S. Jana, Impact of Biofield Treatment on Atomic and Structural Characteristics of Barium Titanate Powder, *Ind. Eng. Manage.*, 2015, **4**(3), 1000166.

51 O. Harizanov, A. Harizanova and T. Ivanova, Formation and characterization of sol–gel barium titanate, *Mater. Sci. Eng., B*, 2004, **106**(2), 191–195.

52 M. R. A. Bhuiyan, M. M. Alam, M. A. Momin, M. J. Uddin and M. Islam, Synthesis and characterization of barium titanate ($BaTiO_3$) nanoparticle, *Int. J. Mater. Mech. Eng.*, 2012, **1**, 21–24.

53 H. Z. Akbas, Z. Aydin, I. H. Karahan, T. Dilsizoglu and S. Turgut, Process control using FT-IR analysis of $BaTiO_3$ from ultrasonically activated $BaCO_3$ and TiO_2, in *Proceedings of the 17th Research World International Conference*, Riyadh, Saudi Arabia, 2016, vol. 11, pp. 27–30.

54 K. V. Karthik, C. V. Reddy, K. R. Reddy, R. Ravishankar, G. Sanjeev, R. V. Kulkarni, *et al.*, Barium titanate nanostructures for photocatalytic hydrogen generation and photodegradation of chemical pollutants, *J. Mater. Sci.: Mater. Electron.*, 2019, **30**(23), 20646–20653.

55 G. N. Almeida, R. N. de Souza, L. F. S. Lima, N. D. S. Mohallem, E. P. da Silva and A. M. A. Silva, The Influence of the Synthesis Method on the Characteristics of $BaTiO_3$, *Materials*, 2023, **16**(8), 3031.

56 K. Suzuki and K. Kijima, Optical Band Gap of Barium Titanate Nanoparticles Prepared by RF-plasma Chemical Vapor Deposition, *Jpn. J. Appl. Phys.*, 2005, **44**(4R), 2081.

57 P. M, S. Pandey, K. R, A. Sati, R. Trivedi, Y. Raviprakash, *et al.*, Uncovering temperature-induced changes in bandgap and electronic heterogeneity in transition metal oxides through optical absorption spectroscopy: A review, *Phys. B*, 2024, **695**, 416485.

58 D. Padalia, U. Kumar, P. Bhandari, J. Dalal, L. Ranakoti and T. Singh, Tuning the structural, optical, and dielectric properties of europium-doped barium titanate ceramics, *J. Mater. Sci.: Mater. Electron.*, 2024, **35**(19), 1375.

59 A. Sagdeo, A. Nagwanshi, P. Pokhriyal, A. K. Sinha, P. Rajput, V. Mishra, *et al.*, Disappearance of dielectric anomaly in spite of presence of structural phase transition in reduced $BaTiO_3$: Effect of defect states within the bandgap, *J. Appl. Phys.*, 2018, **123**(16), 161424.

60 M. Borah and D. Mohanta, Structural and optoelectronic properties of Eu^{2+}-doped nanoscale barium titanates of pseudo-cubic form, *J. Appl. Phys.*, 2012, **112**(12), 124321.

61 J. Lee, H. Jeong and S. Ma, Effects of annealing temperature on structural phase transition and microstructure evolution of hydrothermally synthesized barium titanate nanoparticles, *Mater. Res. Express*, 2022, **9**(6), 065001.

62 N. Zamperlin, R. Ceccato, M. Fontana, A. Pegoretti, A. Chiappini and S. Dirè, Effect of Hydrothermal Treatment and Doping on the Microstructural Features of Sol-Gel Derived $BaTiO_3$ Nanoparticles, *Materials*, 2021, **14**(15), 4345.

63 S. Parida, S. K. Rout, L. S. Cavalcante, A. Z. Simões, P. K. Barhai, N. C. Batista, *et al.*, Structural investigation and improvement of photoluminescence properties in Ba(Zr_xTi_{1-x})O_3 powders synthesized by the solid state reaction method, *Mater. Chem. Phys.*, 2013, **142**(1), 70–76.

64 S. Adireddy, C. Lin, B. Cao, W. Zhou and G. Caruntu, Solution-Based Growth of Monodisperse Cube-Like $BaTiO_3$ Colloidal Nanocrystals, *Chem. Mater.*, 2010, **22**(6), 1946–1948.

65 S. Utara and S. Hunpratub, Ultrasonic assisted synthesis of $BaTiO_3$ nanoparticles at 25 °C and atmospheric pressure, *Ultrason. Sonochem.*, 2018, **41**, 441–448.

66 W. H. Zhang, L. Chen, Y. T. Tao, W. H. Zhang, J. Chen and J. X. Zhang, Raman study of barium titanate with oxygen vacancies, *Phys. B*, 2011, **406**(24), 4630–4633.

67 V. K. Veerapandiyan, H. S. Khosravi, G. Canu, A. Feteira, V. Buscaglia, K. Reichmann, *et al.*, B-site vacancy induced Raman scattering in $BaTiO_3$-based ferroelectric ceramics, *J. Eur. Ceram. Soc.*, 2020, **40**(13), 4684–4688.

68 S. Fuentes, F. Céspedes, P. MuÑoz, E. Chavez and L. Padilla-Campos, Synthesis And Structural Characterization Of Nanocrystalline $Batio_3$ At Various Calcination Temperatures, *J. Chil. Chem. Soc.*, 2013, **58**, 2077–2081.

69 S. Wei Lu, B. I. Lee, Z. Lin Wang and W. D. Samuels, Hydrothermal synthesis and structural characterization of $BaTiO_3$ nanocrystals, *J. Cryst. Growth*, 2000, **219**(3), 269–276.

70 G. De Carvalho Onorato, D. L. A. S. do Amaral, L. F. C. De Oliveira, H. De Mello Brandao and M. Munk, Barium

Titanate Nanoparticles Exhibit Cytocompatibility in Cultured Bovine Fibroblasts: A Model for Dermal Exposure, *Curr. J. Appl. Sci. Technol.*, 2024, **43**(5), 1–10.

71 X. Zhu, J. Wang, Z. Zhang, J. Zhu, S. Zhou, Z. Liu, *et al.*, Atomic-Scale Characterization of Barium Titanate Powders Formed by the Hydrothermal Process, *J. Am. Ceram. Soc.*, 2008, **91**(3), 1002–1008.

72 R. A. Surmenev, R. V. Chernozem, A. G. Skirtach, A. S. Bekareva, L. A. Leonova, S. Mathur, *et al.*, Hydrothermal synthesis of barium titanate nano/microrods and particle agglomerates using a sodium titanate precursor, *Ceram. Int.*, 2021, **47**(7, Part A), 8904–8914.

73 K. Xu, G. Zhu, H. Xu, Y. Zhao, K. Jiang, X. Zhang, *et al.*, The colossal permittivity effect on $BaTiO_3$ induced by different sinter atmosphere, *Appl. Phys. A*, 2022, **128**(12), 1044.

74 L. T. Hudson, R. L. Kurtz, S. W. Robey, D. Temple and R. L. Stockbauer, Photoelectron spectroscopic study of the valence and core-level electronic structure of $BaTiO_3$, *Phys. Rev. B: Condens. Matter Mater. Phys.*, 1993, **47**(3), 1174–1180.

75 Q. Sun, Q. Gu, K. Zhu, R. Jin, J. Liu, J. Wang, *et al.*, Crystalline Structure, Defect Chemistry and Room Temperature Colossal Permittivity of Nd-doped Barium Titanate, *Sci. Rep.*, 2017, **7**(1), 42274.

76 M. M. J. Sadiq, U. S. Shenoy and D. K. Bhat, Synthesis of $BaWO_4$/NRGO-g-C_3N_4 nanocomposites with excellent multifunctional catalytic performance via microwave approach, *Front. Mater. Sci.*, 2018, **12**(3), 247–263.

77 M. Jaffer Sadiq Mohamed and D. Krishna Bhat, A facile microwave approach to synthesize RGO-$BaWO_4$ composites for high performance visible light induced photocatalytic degradation of dyes, *AIMS Mater. Sci.*, 2017, **4**(2), 487–502.

78 D. K. Bhat, H. Bantawal and U. S. Shenoy, Rhodium doping augments photocatalytic activity of barium titanate: effect of electronic structure engineering, *Nanoscale Adv.*, 2020, **2**(12), 5688–5698.

79 S. Chakrabarti, S. Ginnaram, S. Jana, Z.-Y. Wu, K. Singh, A. Roy, *et al.*, Negative voltage modulated multi-level resistive switching by using a Cr/$BaTiO_x$/TiN structure and quantum conductance through evidence of H_2O_2 sensing mechanism, *Sci. Rep.*, 2017, **7**(1), 4735.

80 I. Spasojevic, G. Sauthier, J. M. Caicedo, A. Verdaguer and N. Domingo, Oxidation processes at the surface of $BaTiO_3$ thin films under environmental conditions, *Appl. Surf. Sci.*, 2021, **565**, 150288.

81 A.-C. Iancu, A. Nicolaev, N. G. Apostol, L. E. Abramiuc and C. M. Teodorescu, Reversible oxidation of ethylene on ferroelectric $BaTiO_3$(001): An X-ray photoelectron spectroscopy study, *Heliyon*, 2024, **10**(15), e35072.

82 C.-W. Chiang and J.-H. Jean, Effects of barium dissolution on dispersing aqueous barium titanate suspensions, *Mater. Chem. Phys.*, 2003, **80**(3), 647–655.

83 N. Tymińska, G. Wu and M. Dupuis, Water Oxidation on Oxygen-Deficient Barium Titanate: A First-Principles Study, *J. Phys. Chem. C*, 2017, **121**(15), 8378–8389.

84 G. Ou, Y. Xu, B. Wen, R. Lin, B. Ge, Y. Tang, *et al.*, Tuning defects in oxides at room temperature by lithium reduction, *Nat. Commun.*, 2018, **9**(1), 1302.

85 W. Fan, H. Li, F. Zhao, X. Xiao, Y. Huang, H. Ji, *et al.*, Boosting the photocatalytic performance of (001) BiOI: enhancing donor density and separation efficiency of photogenerated electrons and holes, *Chem. Commun.*, 2016, **52**(30), 5316–5319.

86 B. Zhang, L. Wang, Y. Zhang, Y. Ding and Y. Bi, Ultrathin FeOOH Nanolayers with Abundant Oxygen Vacancies on $BiVO_4$ Photoanodes for Efficient Water Oxidation, *Angew. Chem., Int. Ed.*, 2018, **57**(8), 2248–2252.

87 Q. Yu, D. Liu, R. Wang, Z. Feng, Z. Zuo, S. Qin, *et al.*, The dielectric and photochromic properties of defect-rich $BaTiO_3$ microcrystallites synthesized from Ti_2O_3, *Mater. Sci. Eng., B*, 2012, **177**(9), 639–644.

88 H. J. L. Clabel, I. T. Awan, G. Lozano, M. A. Pereira-da-Silva, R. A. Romano, V. A. G. Rivera, *et al.*, Understanding the electronic properties of $BaTiO_3$ and Er^{3+} doped $BaTiO_3$ films through confocal scanning microscopy and XPS: the role of oxygen vacancies, *Phys. Chem. Chem. Phys.*, 2020, **22**(26), 15022–15034.

89 Q. Guo, T. Gao, M. Padervand, D. Du, K. Zhao, Y. Zhang, *et al.*, Piezo-Photocatalytic Degradation of Tetracycline by 3D $BaTiO_3$ Nanomaterials: The Effect of Crystal Structure and Catalyst Loadings, *Processes*, 2023, **11**(12), 3323.

90 H. Bantawal and D. Krishna Bhat, Hierarchical Porous $Batio_3$ Nano-Hexagons as A Visible Light Photocatalyst, *Int. J. Eng. Technol.*, 2018, **7**(4.5), 105–109.

91 M. U. Draz, M. Zia Ul Haq, A. Hayat and H. Ajab, An ALP enzyme-based electrochemical biosensor coated with signal-amplifying $BaTiO_3$ nanoparticles for the detection of an antiviral drug in human blood serum, *Nanoscale Adv.*, 2024, **6**(2), 534–547.

92 R. A. Sobh and H. S. Magar, Innovative formulation of a functional nano-copolymer derived from glycidyl methacrylate and acrylonitrile as an exceptionally sensitive and selective electrochemical sensor for folic acid detection in pharmaceutical and food samples, *Nanoscale*, 2025, **17**(31), 18359–18376.

93 M. Uçar, K. Polat, A. O. Solak, M. Toy and M. L. Aksu, The electrochemical behaviour of 2′-halogenated derivatives of 4-methoxyazobenzene at a mercury electrode, *Dyes Pigm.*, 2010, **87**(1), 55–61.

94 H. A. Ávila, L. A. Ramajo, M. M. Reboredo, M. S. Castro and R. Parra, Hydrothermal synthesis of $BaTiO_3$ from different Ti-precursors and microstructural and electrical properties of sintered samples with submicrometric grain size, *Ceram. Int.*, 2011, **37**(7), 2383–2390.

95 M. F. Mehmood and A. Habib, Hydrothermal Synthesis and Structural Characterization of $BaTiO_3$ Powder, *The Nucleus*, 2023, **60**(2), 168–173.